In-situ vertical characteristics of optical properties and heating rates of aerosol over Beijing

Ping Tian[1], Dantong Liu[2*], Delong Zhao[3], Chenjie Yu[4], Quan Liu[1], Mengyu Huang[1], Zhaoze Deng[5], Liang Ran[5], Yunfei Wu[6], Shuo Ding[2], Kang Hu[2], Gang Zhao[7], Chunsheng Zhao[7], Deping Ding[1,3]

1. Beijing Key Laboratory of Cloud, Precipitation and Atmospheric Water Resources, Beijing, 100089, China.

2. Department of Atmospheric Science, School of Earth Sciences, Zhejiang University, Hangzhou, Zhejiang, 310027, China.

3. Field Experiment Base of Cloud and Precipitation Research in North China, China Meteorological Administration, Beijing, 100089, China.

4. Centre for Atmospheric Sciences, School of Earth and Environmental Sciences, University of Manchester, Manchester, M139PL, UK

5. Key Laboratory of Middle Atmosphere and Global Environment Observation, Institute of Atmospheric Physics, Chinese Academy of Sciences, Beijing, 100029, China.

6. CAS Key Laboratory of Regional Climate-Environment for Temperate East Asia, Institute of Atmospheric Physics, Chinese Academy of Sciences, Beijing, 100029, China.

7. Department of Atmospheric and Oceanic Sciences, Peking University, Beijing, 100871, China

Corresponds to: Dantong Liu (dantongliu@zju.edu.cn)

Abstract. Characterizing vertical profiles of aerosol optical properties is important because only relying on the surface or column-integrated measurements is unable to unambiguously constrain the radiative impacts of aerosol. This study presents series of vertical profiles of in-situ measured multi-wavelength optical properties of aerosols during three pollution events from Nov. to Dec. 2016 over Beijing region. For all pollution events, the clean periods (CP) before pollution initialization showed a higher scattering Ångström exponent and a smaller asymmetry parameter (g), and relatively uniform vertical structures. The heavy pollution (HP) periods showed increased particle size, causing these parameters to vary in the opposite way. During the transition periods (TP), regional transport of aged aerosols at upper level was found. The AERONET aerosol optical depth (AOD) matched the in-situ measurements within 10 %, however the AERONET absorption optical depth (AAOD) was 10-20 % higher than in-situ measurements, and this positive discrepancy increased to 30 % at shorter wavelength. The absorption of brown carbon (BrC) was identified by increased absorption Angström exponent (AAE), and the heating rate of black carbon (BC) and BrC was calculated by computing the wavelength-dependent absorption coefficient and actinic flux by the radiative transfer model. BC and BrC had a heating rate up to 0.18 K/h and 0.05 K/h in the planetary boundary layer (PBL) respectively during the pollution period. The fraction of BrC absorption increased from 12 % to 40 % in the PBL from CP to HP period. Notably, higher contribution of BrC heating was found above the PBL under polluted condition. This study gives a full picture of shortwave heating impacts of carbonaceous aerosols during different stages of pollution event, and highlights the increased contribution of BrC absorption especially at higher level during pollution.

1. Introduction

The optical properties of aerosol, which is how aerosol scatters or absorbs solar radiation, have caused important radiative impacts on earth system (IPCC2013). The optical properties depend on the particle size (Bergin et al., 2001), refractive index (Ebert et al., 2002; Quinn, 2002) and mixing state of aerosols. There are still large uncertainties in evaluating the radiative forcing of aerosol especially in east Asia region due to lack of information on vertical distribution of these parameters (Liao and Seinfeld, 1998; Ramanathan et al., 2001; Li et al., 2017). Previous studies showed that the surface observation or column-integrated measurements may not provide sufficient information to derive vertical profiles of aerosol optical properties (Andrews et al., 2011; Rosati et al., 2016). Modelling studies found the radiative forcing impact is sensitive to the aerosol vertical distribution (Haywood et al., 1998), and especially for the absorbing aerosol such as black carbon (BC) will exert different climatic impacts depending on the location of aerosol layer (Yu et al., 2002; Ban-Weiss et al., 2011; Wilcox et al., 2016). Even though most aerosol was contained inside the planet boundary layer (PBL), the climatic sensitivity to absorbing aerosol rapidly increases with altitude (Ramanathan et al., 2001; Hodnebrog et al., 2014; Nazarenko et al., 2017). Absorbing aerosol above the PBL has the potential to suppress the PBL development and enhance the inversion cap at top of the PBL (Ding et al., 2016; Wang et al., 2018c), further execrating the pollution. However, this impact depends on the location of the absorbing layer which may also promote the convection by heating the layer above (Koch and Del Genio, 2010; Yu et al., 2019). It is therefore important to characterize the vertical profile of absorbing component in the atmosphere in order to understand its influence on atmospheric thermodynamics.

The North China Plain (NCP) has raised great attention in recent decades because of the severe air pollution and high frequency of haze days. The causes of pollution have been widely investigated through surface measurements (Zhang et al., 2013; Zhang et al., 2015; Zhong et al., 2018), however only limited studies have considered the evolution of pollutants in vertical direction (Tian et al., 2019; Wang et al., 2018a). It was found the surface aerosol concentration over Beijing not only depended on the emission but the vertical structure of aerosol distribution, which was largely dependent on local and synoptic meteorological conditions (Ran et al., 2016a; Zhao et al., 2019a), such as the mountain chimney effect

over Beijing region may introduce enhanced aerosol loading to high ~~level~~ (Chen et al., 2009). The light-absorbing aerosol mainly includes the species of black carbon (Bond et al., 2013), brown carbon (Lack and Cappa, 2010) and dust (Klingmüller et al., 2019), which have different spectral sensitivities to solar radiation. Different aerosol components dominate at different environments, and the heating rate caused by various aerosol sources has been studied over the world, e.g. for the anthropogenic sources over north America (Gao et al., 2008; Sahu et al., 2012; Liu et al., 2015b), Europe (Ferrero et al., 2014; Ferrero et al., 2018) and south Asia (Chakrabarty et al., 2012; Shamjad et al., 2015), and biomass burning sources over north and south America (Saleh et al., 2015; Zhang et al., 2017). However ~~the data is still sparse~~ regarding the vertical structures of heating rate, in addition to that, the heating was mostly evaluated using the measurement on the surface (Mallet et al., 2008; Wang et al., 2009) rather than using directly measured vertical profile. The calculation ~~was~~ performed for single species such as BC or BrC but most did not consider the co-impacts of all species (Chakrabarty et al., 2012; Chung et al., 2012; Shamjad et al., 2015). In the lower free troposphere, the ~~heating rate of aerosol in interacting~~ with boundary layer dynamics has raised much attention recently, as it may play important role in ~~de~~pressing boundary layer development hereby exacerbating the local pollution (Li et al., 2017). The heating rate caused by light absorbing aerosol was reported to vary as a function of height and range at 0.3-2.1 K/day for the polluted PBL over Europe (Kedia et al., 2010; Ferrero et al., 2014; Ferrero et al., 2018), and 0.3-2.5 K/day for south Asia (Tripathi et al., 2007; Ramana et al., 2007; Ramachandran and Kedia, 2010; Chakrabarty et al., 2012); ~~but~~ limited reports ~~for the region of polluted~~ east Asia.

This study chose three typical pollution events occurring in wintertime over Beijing, and performed continuous flights on daily basis for each event. The vertical profiles of multi-wavelength aerosol optical properties were in-situ characterized, accounting for all stages during pollution events from pollution starts, full development and cease. The directly measured optical parameters were used as inputs for radiative transfer calculation, hereby the heating rate of light-absorbing aerosols, including black and brown carbon (BrC) was estimated. The results here provide a full picture of vertical profiles of aerosol optical properties over Beijing region and investigate the radiative forcing effect of aerosol during the heavy pollution events.

2. Instrumentation and data analysis

A Kingair 350ER turbo aircraft in Beijing weather modification office was employed for the in-situ measurements over Beijing during the 2016 winter in this study. Meteorological parameters including the temperature, relative humidity, pressure, wind direction and wind speed with a time resolution of 1 s were measured by the Aircraft Integrated Meteorological Measurement System (AIMMS-20, Aventech Research Inc, Canada), which was calibrated annually. The aerosol instrumentation inside the cabin was connected to an isokinetic inlet (Model:1200, Brechtel Inc, USA), which can deliver particle with a high transport efficiency (90%) for sub-micrometer particles. The ~~maintained~~ room temperature (25 ºC) in the cabin had self-drying effect when the temperature inside was higher than outside the cabin, in addition to which, a silicate ~~direr~~ was ~~utilized~~ ~~ahead~~ of all instruments to maintain ~~the~~ sampling RH lower than 40%.

In-situ measurements of aerosol optical properties were performed during three pollution events over Beijing in Nov. 15th to Dec. 21th 2016, including 14 flights covering the start, development and cease stage for each pollution event. All flights were conducted around midday when the PBL was well developed. Table 1 summarizes the information of each flight. In order to compare the AOD from AERONET and calculate the vertical heating rates, only the cloud-free vertical profiles are used. In this study, three flights (20161117 12:00, 20161117 15:00, 20161118 12:00) were observed with cumulus clouds (Table 1). The in-cloud data in this study was screened out according to the in-situ measured cloud number concentration and liquid water content, with a total number concentration of more than 10 cm^{-3} and liquid water of more than 0.001 g m^{-3} are not included in the following analysis (Deng et al., 2009). A micro pulse lidar (MPL, Sigma Inc, USA) was employed to measure the temporal evolution of aerosol extinction vertical profiles, and the vertical wind profile was measured by a wind profile radar with a vertical resolution of 150 m.

2.1 Aerosol optical properties

The aerosol scattering (σ_{sca}) and hemispheric backscattering (σ_{bsca}) coefficients at λ=450 nm, 525 nm, and 650 nm were measured by an integrating nephelometer (Aurora3000, Ecotech Inc, Australia), and the

flowrate of Aurora3000 was maintained at 4 L/min during flight. The baseline of Aurora3000 in real time was corrected for Rayleigh scattering of gas molecule at different air pressure (Fig. S1). In addition, the σ_{sca} and σ_{bsca} at all wavelengths were corrected for truncation affects (Anderson and Ogren, 1998;Müller et al., 2009).

The scattering Ångström exponent (SAE) measures the wavelength dependence of σ_{sca} assuming a power relationship with λ, expressed as:

$$SAE = -\frac{\ln(\sigma_{\lambda 1}/\sigma_{\lambda 2})}{\ln(\lambda_1/\lambda_2)}, \quad (1)$$

where $\sigma_{\lambda 1}$ denotes the σ_{sca} at λ_1, the value of SAE could also be used to reflect particles size with larger particles showing a smaller SAE (Carrico et al., 1998).

The asymmetry parameter (g) is obtained from measured backscattering fraction according to the empirical function from Andrews et al. (2006).

$$g = -7.143889 \cdot \beta^3 + 7.4633439 \cdot \beta^2 - 3.9356 \cdot \beta + 0.9893, \quad (2)$$

where β is the hemi-spherical backscatter fraction ($\sigma_{bsca}/\sigma_{sca}$) measured by the Aurora3000.

The absorbing coefficient (σ_{abs}) at different wavelengths (370, 470, 520, 590, 660, 880, and 950nm) was measured by an Aethalometer (AE33, Magee Scientific Inc, USA) (Hansen, 2005). The flowrate of AE33 was maintained at 4 L/min below 3000 m. The shadowing effect of the AE33 was corrected by the two spot measurements with different attenuation (Drinovec et al., 2017). The multiple scattering artifact of AE33 was corrected by measuring the ambient aerosol in parallel with photoacoustic spectrometer (PASS3, DMT Inc, USA), and the latter is independent of the filter artifacts. The PASS3 was calibrated using the NO_2 and BC standard. (Arnott et al., 2005). Fig. S2 shows the two weeks' ambient measurements between AE33 and PASS3 at three overlapped wavelengths. Multiple scattering correction factor of 2.88 was consistently found at three λ, which was applied to correct the AE33 measurement.

The absorbing Ångström exponent (AAE), which can weight the absorption at different wavelength, is calculated using power fitting at seven wavelengths.

$$\sigma_{abs}(\lambda) = \sigma_{abs,0}\,(\lambda/\lambda_0)^{AAE}, \quad (3)$$

We estimated the σ_{abs} of brown carbon (BrC) assuming that BC is the only absorber at λ=950 nm, then the absorption of BC at other wavelengths was extrapolated by assuming an AAE of 1 (Kirchstetter et al., 2004;Lack et al., 2013;Massabò et al., 2015), and the contribution of BrC at each wavelength was obtained by subtracting the BC absorption from the total absorption (Schnaiter et al., 2005;Liu et al., 2015a). It should be noted that previous studies point out the AAE_{BC} may be less than 1, thus assuming $AAE_{\mathbf{BC}}$=1 may lead to underestimation of BrC contribution (Gyawali et al., 2009; Lack and Cappa, 2010; Feng et al., 2013). We therefore consider the results reported here is the lower bound of BrC contribution.

The single scattering albedo (SSA) is the ratio of the scattering coefficient over the extinction coefficient (σ_{ext}) at a given wavelength.

The parameters σ_{sca}, σ_{abs}, and σ_{ext} are reported ~~as~~ standard temperature and pressure (STP, 1013.25~~hpa~~ , 273.15K) for direct comparison at different altitudes among flights. Note that to compare with the AERONET results and for the radiative transfer calculation (as detailed in the following), these parameters in ambient conditions are used.

Column aerosol optical properties during the aircraft observation period were obtained from Aerosol Robotic Network (AERONET) sun-photometer network (Che et al., 2009; Xia et al., 2008), where the site (AERONET BEIJING_PKU) was about 10 km away from the location of vertical profiles. The measurement of σ_{ext} was up to 2500m above which the aerosol concentration was low enough to be below the instrument lower detection limit. Given the very low concentration above 2500m, the value on top of 2500m was used to reconstruct the vertical profile up to 5000m. After that the σ_{ext} from 2.5-5 km only accounted for 1-2 % of the integrated columnar extinction.

To evaluate the potential influence of particle hygroscopicity on optical properties, the aerosol hygroscopic growth parameterization (f(RH)) was used to calculate the enhancement of σ_{sca} under ambient RH. This function was previously measured by Zhao et al. (2019b) over Beijing region, expressed as:

$$f(RH) = a \cdot (1 - RH/100)^{-\gamma(RH/100)} \quad (4)$$

where f(RH) was obtained by a comparison between a dry and humidified nephelometer in parallel. a

/ γ was 0.930 / 0.329, 0.971 / 0.372, and 0.988 / 0.356 for clean, moderate, and heavy pollution period, respectively, according to the study.

The RH influence on g was calculated according to Zhao et al. (2018), expressed as:

$$g(RH)/g(RH < 40\%) = a \cdot (1 - RH/100)^{-\gamma(RH/100)} \quad (5)$$

where a / γ was 0.9984 and 0.0849.

The resulting σ_{sca}, σ_{ext}, SSA, and g are all calculated for the hygroscopicity influence.

2.2 Radiative transfer calculation

The atmospheric irradiance and actinic flux using the pseudo-spherical version of the Discrete Ordinates Radiative Transfer Code (DISORT), as implemented in the libRadtran software package (Emde et al., 2016). The ~~aircraft~~ in-situ measured vertical profiles of AOD, single scattering albedo (SSA) and g are used as inputs, and the other input parameters for the radiative transfer calculation ~~is~~ summarized in Table 2. The calculation is performed for clear-sky condition only, thus the flights experiencing low-level clouds are not included in the calculation. The direct, upward diffuse, and downward diffuse irradiance and actinic flux (AF, in mWm^{-2}) at λ = 250-2550 nm are calculated. The calculation of AF is performed with and without aerosol input (AOD is set to zero) to evaluate the aerosol net impact. The heating rate is only calculated with considering the in-situ measured AOD. The spectral instantaneous absorbing power of BC (A_{BC}) or BrC (A_{Brc}) can be calculated by multiplying the absorption coefficient of BC (or BrC) and AF at specified λ, then integrating all λ will obtain the total absorbing power (Gao et al., 2008; Emde et al., 2016), expressed as:

$$A_{BC\ or\ BrC} = \int_{250nm}^{2550nm} AF(\lambda) \cdot \sigma_{BC\ or\ BrC}(\lambda)\, d\lambda, \quad (6)$$

By assuming no radiative loss of solar energy and the heat absorbed by aerosol is fully transferred to the surrounding air, the instantaneous heating rate of BC or BrC to ambient air is hence calculated as:

$$H_{BC,BrC} = A_{BC,BrC}/(\rho \cdot C_p), \quad (7)$$

where ρ and C_P are the air mass density (kg/m^3) and heat capacity (1.007 J/g*K), respectively. The profiles of aerosol optical properties influenced by hygroscopic growth (as calculated above) is also input in the calculation to work out its influence on heating rates.

3. Results and discussions

3.1 Overview and the pollution events

Three pollution events from Nov. 15th to 18th (Case 1), Dec .10th to 12th (Case2), and Dec. 16th to 19th (Case 3) in 2016 were captured. Figure 1 shows the temporal evolution of surface $PM_{2.5}$, AOD (AAOD) constrained by in-situ aircraft measurements and from AERONET, and vertical profiles of σ_{ext} and wind information during Case 1 pollution event. The other two events are shown in Fig. S3 and Fig. S4. Aircraft vertical profiles were performed on daily basis as the flight time indicated by vertical bars (Fig. 1). Each pollution event was classified as pollution initialization, development and peak pollution periods, corresponding to the pollution levels as clean period (CP, $PM_{2.5,\,surface} < 35$ μg/cm^3), transition period (TP, 35 μg/cm^3 < $PM_{2.5,\,surface} < 200$ μg/cm^3) and heavy pollution (HP, $PM_{2.5,\,surface} > 200$ μg/cm^3). Three flights (20161117 12:00 , 20161117 15:00, 20161118 12:00) experienced boundary layer cloud (Fig. 1c), as indicated by the intensive extinction on top of the PBL. There were 3, 4 and 4 profiles in clear sky for LP, TP and HP period respectively (as detailed in Table 1). As Fig. 1b shows, wind sheer in both wind speed and direction appeared on top of PBL, consistent with the vertical distribution of σ_{ext} observed by a lidar (Fig. 1c). During LP, wind profiles (Fig. 1b) showed dominant northwesterly wind with high wind speed throughout the column, enhancing the pollutant dispersion in more developed PBL (Fig. 1c). During TP, the southerly air flow dominated and the $PM_{2.5}$ mass concentration underwent a rapid increase from 30 to 100 μg m^{-3} in several hours. During HP, the windspeed was relatively low at all altitudes, maintaining the $PM_{2.5}$ mass concentration at a high level.

Figure 2 summarized the in-situ measured meteorological parameters at different stages of pollution events. The height of PBL (PBLH) was determined by considering a variety of factors. Firstly, a stable potential temperature (θ) (Fig. 2d-f) with vertical gradient $d\theta/dz$ < 5 K/km in the PBL indicated an

sufficient convective mixing (Su et al., 2017), with an apparent positive gradient above the PBL indicating a stable layer (Petra Seibert, 2000). Secondly, there was usually a temperature inversion on top of the PBL (Fig. 2a-c). During the CP, the weak temperature inversion (~0.15K/100m) on top of the PBL allowed pollutants to penetrate the PBL and disperse in a higher atmospheric column (Fig. 2b). This inversion was significantly enhanced for the TP and HP periods, to 0.9K/100m and 0.7K/100m respectively. The large increase of the inversion during flight 20161211 was caused by regional transport from the south, when lower-latitude warmer air mass was imposed onto the measurement point (Tian et al., 2019). Additionally, the PBLH decreased gradually as pollution continued during the pollution event, in line with the enhanced aerosol concentration in the PBL. The moisture had similar features that a lower moisture content showed when lower pollution level and vertically efficiently dispersed, whereas stronger inversion also trapped the moisture inside the PBL, leading to a positive vertical gradient with the maximum RH showing on top of the PBL. There were some regional transport influences under TP, resulting in enhanced RH when airmass was advected from the south (Fig. 2f).

3.2 Vertical profile of σ_{ext}, σ_{sca} and σ_{abs}

Figure 3 shows the vertical distribution of aerosol optical properties including extinction (σ_{ext}), scattering (σ_{sca}) and absorbing (σ_{abs}) coefficients. Different structures of vertical profiles were observed for CP, TP and HP periods. During CP, aerosol concentration was low and showed uniform mixing inside the PBL, with the σ_{ext}, σ_{sca} and σ_{abs} ranging from 220-270 Mm^{-1}, 180-240 Mm^{-1}, and 30-50 Mm^{-1}, respectively. The backward trajectories for the CP showed that the air masses were from the northwestern low emission region (Fig. S5). TP showed about 4-fold increase of σ_{ext} compared to the CP. During TP, the σ_{ext}, σ_{sca} and σ_{abs} had large variation inside the PBL, ranging from 325-1435 Mm^{-1}, 300-1275 Mm^{-1}, and 45-160 Mm^{-1}, respectively, and the mean PBLH decreased to 200-500 m. During these pollution accumulation periods (before the pollution reached peak level), two contrast vertical structures was observed. One showed well-mixing in the PBL but declined concentration in the free troposphere (FT) (e.g. flight 20161115PM and 20161210) (Fig. 3a). The other one had the increased aerosol layer on top of the PBL, and showed positive vertical gradient for all optical properties at certain level (e.g. flight 20161116 AM, 20161211 and

20161216) (Fig. 3b). The former was because of the mostly cleaner northwesterly air mass and higher wind speed influencing the layer above the PBL, while the latter resulted from the southwesterly regional transport (Tian et al., 2019).

During HP period, most flights showed consistent exponentially-declined vertical profile patterns, and the PBLH was even lower than that in TP (Fig. 2f). The stronger temperature inversion (Fig. 2c) and lower wind speed (Fig. 1b) inside the PBL led to high stability of the PBL and promoted the pollutant accumulation. The aerosol concentration was largely enhanced towards the surface and sharply declined above the PBL. Interestingly, the absorption showed higher degree of negative vertical gradient than the scattering at λ=440nm, which reflected the different sources and mixing ratios of absorbing and non-absorbing aerosols. The surface emission tends to contain more primary sources of absorbing particles such as BC and BrC, while enhanced secondary aerosol formation at upper level may add additional aerosol extinction.

The vertical profiles of σ_{sca} and σ_{abs} during HP can be fitted as:

$$\sigma_{sca} = \sigma_{sca,0} \cdot \exp(-a * H); \ \ a = 0.0012 \pm 0.0001, \quad (8)$$

$$\sigma_{abs} = \sigma_{abs,0} \cdot \exp(-b * H); \ \ b = 0.0015 \pm 0.0001, \quad (9)$$

where σ_0 represent the surface value of σ_{sca} and σ_{abs}, and H is the altitude. The a and b are the parameters defining the changing rate with the altitude. This parameterization could be used to represent the vertical structure of optical properties under heavy pollution condition.

The hygroscopic effect on aerosol vertical profiles was mainly controlled by the ambient RH (shown in blue lines in Fig. 3). For most of the flights, the hygroscopic effect could be neglected due to low RH (< 50%) (Fig. 2). For some of the flights (20161211), σ_{sca} and σ_{ext} especially at top of the PBL could be enhanced by a factor of 1.3.

3.3 Vertical profile of SSA, SAE, AAE and g

Figure 4 shows the vertical profiles of *SSA, SAE, AAE,* and *g* for all the flights during different stages of

pollution events. Overall, the SSA showed two modes inside the PBL. Under the CP, SSA for most flights was populated at 0.85, and had less variation throughout the column in the PBL. Flight 20161115AM showed a strong elevation of SSA (0.94) at 2200 m (Fig. 4a), which may be influenced by a dust layer (as further discussed below). SSA showed positive vertical gradient for the TP and HP inside the PBL, i.e. from the surface to the PBLH, the mean SSA increased from 0.85 to 0.91 and from 0.87 to 0.92 for TP and HP period, respectively. This indicates the reduced fraction of absorbing particles, in turn suggesting an enhancement of secondary production of non-absorbing particles. There were a few profiles featuring with large enhancement of SSA (>0.95, for flight 20161211) at high altitude (Fig. 4b), and backward trajectory analysis (Fig. S5) showed that these resulted from regional transport when more aged pollutants were advected to a high altitude. The SSA in the FT was mostly higher than that in the PBL and maintained at 0.9-0.95 for TP and HP, suggesting a lower absorbing particle fraction at higher altitude. Comparing among different stages during pollution event, it could be concluded that at the initialization stage of pollution when the total PM was relatively low, a lower SSA exhibited, while the increase of pollution level added more secondary species, hence increasing SSA. This trend was consistent with previous ground studies in Beijing (He et al., 2009; Jing et al., 2011).

The SAE reflects the particle size with larger size having a smaller SAE. A decreasing SAE was shown for increasing pollution levels inside the PBL (Fig. 4), i.e., from CP to HP, the SAE in the PBL showed an average value of 1.74, 1.45, and 1.21, respectively. For most of the profiles, SAE showed enhancement at higher altitude. This means smaller particle sizes at high altitude, which may result from a higher scavenging efficiency for larger particles where smaller particles remained un-scavenged in the upper level (Liu et al., 2009). These was an exception of flight 20161211, when regional advection transported larger and aged particles to the higher altitude. The particle size also corresponded with asymmetry parameter (*g*, Fig. 4j-i), with larger particle presents more fraction of forward scattering (larger *g*). Note that there only one flight (flight 20161211) under RH > 80 %, where the particle hygroscopicity had appreciable influence on *SSA* (increased by 0.05), *SAE* (decreased by 0.2) and *g* (increased by 0.1).

AAE reflects the degree of absorption towards shorter wavelength, such as the presence of BrC will enhance the absorption in the UV. A lower AAE 1.2 ± 0.2 was shown for the CP (Fig. 4g), but increased to 1.56 ± 0.3 for TP in the PBL (Fig. 4h), and additional higher mode of AAE showed at 1.8-2.0 for the

HP period (Fig. 4i). There was weak variation of AAE for CP throughout the column, but became largely spreading for TP, i.e., with either positive or negative vertical gradient at different levels. Notably, the AAE showed consistent positive vertical gradient for most of the HP profiles (Fig. 4i). This implied the enhancement of BrC contribution at higher altitude for polluted troposphere. Flight 20161115AM showed a notably increased AAE up to 2 at altitude 2 km (Fig. 4g), which may reflect the influence of dust (Cazorla et al., 2013). The ground AAE had strong seasonal variation with winter normally showing a higher AAE due to higher emissions of solid fuel burning (Sun et al., 2017; Wang et al., 2018b). However, there is still lack of results on the vertical characteristics of AAE due to limited measurements, and the results here highlight the enhancement of BrC at high level, mainly for polluted environment.

3.4 Comparison of column integrated and in-situ constrained AOD/AAOD

To compare the AOD and AAOD between AERONET and that constrained by in-situ aircraft measurements, the AERONET data was chosen to match with the aircraft profiles in time (±3h) and location (within 10 km) (the PEK site). The comparison was performed at overlapped wavelengths (440nm, 675nm, and 870nm) between AERONET and aircraft instruments. As Fig. 5a-c shows, high correlation (R^2 > 0.95) was found between columnar and in-situ measurement. In particular, the correlation was ~~most unit under~~ dry condition (RH < 40%), while the AERONET was about 10-20% higher than in-situ measurement ~~when~~ RH > 60%. Improved agreement was achieved by 8-15% if considering aerosol hygroscopic growth (open circle in Fig. 5a-c), despite that in-situ constrained AOD was still 2-5% lower than AERONET after the hygroscopic correction.

Figure 5g-i shows at three wavelengths the AAOD had lower correlations between both methods compare to AOD, with R^2= 0.75, 0.58, and 0.49 at 440 nm, 675 nm, and 870nm, respectively. The columnar AAOD was overall about 10-25% higher than in-situ measurement, and this AERONET AAOD overestimation was higher under higher AOD condition. This is consistent with previous findings conducted over US that the ~~retrieved~~ AAOD from AERONET was biased higher when compared to in-situ measurement (Andrews et al., 2017).

Note that there was better agreement during CP, when lower pollution level and lower RH (shown in blue dots). This suggests a lower moisture and less AOD interface may improve the agreement of AAOD. As previous studies pointed out that the retrieval of the AERONET was sensitive to the variation of aerosol vertical distribution (Torres et al., 2014). We speculate that the better agreement for CP was due to the vertically homogeneous distribution of aerosol optical properties, and larger bias for CP and HP periods might be caused by the significant variations of the vertical profiles. Other factors like the aerosol hygroscopic growth under higher RH may introduce factors in enhancing the absorption, e.g. more lensing effect on BC absorption via thicker and moisture coating (Wu et al., 2017). Though this study is not able to rule out the exact influencing factor in causing this discrepancy, an overestimation of 25% in the AERONET AAOD under polluted condition is shown for the dataset here.

3.5 Heating impacts of BC and BrC

Figure 6 shows vertical profiles of irradiances from radiative transfer calculation using in-situ measurements as model inputs (Table 1). The results show that the presence of aerosols reduced the direct irradiance reaching the surface (Fig. 6a-c) but increased the upward diffuse (Fig. 6d-f) and downward diffuse irradiances, especially above the PBL (Fig. 6g-i). The direct irradiance on the surface ranged from 1×10^9 to 3.5×10^9 mW m^{-2}, with an average of 2.2×10^9 mW m^{-2} during CP (Fig. 6a), which was about two-fold and three-fold larger than that during TP (Fig. 6b) and HP period (Fig. 6c), respectively. The combined direct, diffuse upward and downward irradiance which forms the actinic flux (AF), showed an enhancement above the PBL and a reduction within the PBL (Fig. 7a-c), but to what extent the enhancement or reduction occurred depends on the aerosol vertical profile. The vertical gradient of AF was slightly modified by aerosol loadings during CP, whereas for the TP and HP, aerosol effects caused AF about two times smaller within the PBL and 20 % larger above the PBL, leading to an increased vertical gradient of AF. The AF received at lower level was reduced by up to 10 % by incorporating the aerosol hygroscopicity influence (Fig. 7) due to enhanced AOD, and AF was further redistributed to give larger vertical gradient (Fig. 7a-c).

The vertical profiles of absorbing power and heating rate of BC are shown in Fig. 7d-f. Vertically homogeneous BC heating rates of 0.05 K/h was found inside the PBL during CP (Fig. 7d). During the

regional transport cases (flight20161211 and flight20161216) for TP, positive vertical gradient (increase with increasing altitude) of BC heating rates was observed, and as high as 0.1 K/h heating rate could occur at top of the PBL height (Fig. 7e). During the HP period, negative heating rate (decrease with increasing altitude) of BC was found except for one flight on 20161212 in Case 2, and the BC heating rate at the surface could reach as high as 0.15 K/h (Fig. 7f). The reason causing negative vertical gradient of BC heating rate was the higher degree of negative gradient of σ_{abs} (Fig. 3i) than the positive gradient of AF (Fig. 7). The results here show that the atmospheric heating by aerosol was mainly inside the PBL and for polluted period the BC-induced heating was 0.05-0.17 K/h, generally consistent with previous studies over the polluted Asia region, with 0.02-0.17 K/h (Ramana et al., 2007; Ramana et al., 2010; Kedia et al., 2010).

The contribution of BrC to absorbing power and heating rates was computed as the integrated portion of absorption over visible wavelength (370–950nm in this study) by subtracting the BC absorption. Figure 7g-i shows the vertical profile of BrC heating rate. Continuously increase of BrC heating rate in the PBL was observed from CP to HP, with mean heating rate of 0.02 K/h, 0.03 K/h, and 0.05 K/h during CP, TP and HP respectively. Though the BC was the main contributor to the heating in the PBL, the heating of BrC was more evenly distributed and could be comparable with the BC heating rate at high altitude especially during HP period (Fig. 7i). The contribution of BrC to the total absorption was reported to be 10-27 % over polluted region of Europe (Ferrero et al., 2018) and south Asia (Chung et al., 2012; Shamjad et al., 2015), in general consistent with results during polluted periods here.

Corresponding with the aerosol hygroscopicity influence on the actinic flux, the heating rate showed lowered intensity but enhanced vertical gradient for the flights with high ambient RH (Fig. 7b). The vertical gradient of the overall heating rate from absorbing components, i.e. increase or decrease heating rate with altitude, will importantly determine the influence on atmospheric stability. If the heating occurred near surface (Case 3), the lower layer will be heated leading to enhanced convective mixing (Sühring et al., 2014; Petaja et al., 2016); whereas if heating was above the PBL (Case 2), an increase of temperature inversion will occur hence inhibit the PBL development trapping the pollutants in the PBL (Chakrabarty et al., 2012; Tripathi et al., 2007). This study showed positive vertical gradient for 30 % of the flights especially under high pollution, and in particular during regional transport when pollutants

were advected from outside of Beijing and showed elevation of absorption at higher altitude (Fig. 8). The rest of the flights showed highly accumulated aerosol concentration near surface, also found by a previous study (Ferrero et al., 2014), when BC ~~wound~~ potentially promoted the dispersion in the PBL and decreased its stability.

3.6 The importance of BrC heating effects

Figure 8 shows the measured absorption coefficient of BrC and BC inside and above the PBL at different λ for CP, TP and HP period, respectively. The results suggested that both σ_{abs} of BC and BrC increased with the pollution level, e.g. the σ_{abs} at λ= 440nm was 42.8 Mm^{-1} and 7.2 Mm^{-1} on average in the PBL and above the PBL respectively under HP period, and was 4.7 Mm^{-1} and 1.3 Mm^{-1} for LP. The contribution of BrC to total σ_{abs} was found to increase from CP to HP period (Fig. 8c, f). This is in line with previous studies in urban Beijing that more BrC contribution to total absorption was found under higher pollution level (Xie et al., 2019;Ran et al., 2016b), suggesting the important role of BrC on absorption under polluted condition.

The contribution of BrC to total heating rate showed notably different vertical structures. During CP, all profiles showed consistently low BrC contribution throughout the column, with about 7 % at the surface and 9 % in the FT (Fig. 8g). This means the low primary emission or the emission after being diluted by clean air mass did not contained large fraction of absorbing organics. During TP, BrC contribution inside the PBL increased to 22 % and showed considerable variation at higher level (Fig. 8h). During HP period, the surface contribution was comparable with that in TP, but showed remarkably enhanced BrC heating contribution at higher altitude, with a vertically increasing rate of 1.5 %/m in the PBL and reached as high as 45 % in the LFT. The higher heating contribution of BrC at higher altitude means the BrC absorption played an important role in heating at upper level, which may enhance the temperature inversion at that level hereby inhibit the convective mixing under the heated layer.

By comparing the BrC heating contribution at the surface, there was an increase from CP to TP, however, not from TP to HP. This suggests the primary emission will increase the BrC fraction from CP to TP, but for even more pollution environment from TP to HP, the primary emission may provide limited further

increased faction of BrC. The primary BrC may result from a range of combustion sources, with the polluted region at the south of Beijing may contain higher fraction of residential coal burning sources (Sun et al., 2017; Xie et al., 2019) which may influence the Beijing region under polluted period. The relatively consistent BrC contribution at ~20 % from TP to HP suggested the relatively uniform BrC profiles for the primary sources. During TP, the BrC contribution above the PBL had rarely been above 30 % (Fig. 8h), however during HP, there was further enhancement of BrC contribution up to 45 % above the PBL (Fig. 8i). Note that there was no direct injection of biomass burning plume to the high altitude during the study period, the higher portion of BrC absorption above the PBL during HP may be formed through secondary production in addition to the primary source contribution. As Fig. 7a-c shows, there was more intensive actinic flux received at higher altitude and this will promote the photochemical reactions of gas-phase species, allowing more secondary formation of aerosol which may contain a fraction of BrC (Feng et al., 2013;Nakayama et al., 2013). Previous studies also found promoted BrC formation with light source under certain RH (Nguyen et al., 2012; Updyke et al., 2012; Laskin et al., 2015; Zhao et al., 2015). The positive gradient of BrC heating contribution was more likely resulted from enhanced RH from the surface to the top of PBL (Fig. 2i), because increased moisture will promote the aqueous reaction and gas-to-aerosol conversion which may also form part of the BrC observed here (Ervens et al., 2011;Nakayama et al., 2013). The secondary formation of BrC also requires the inorganic or VOC precursors being transported to the high level, therefore the enhancement of BrC mostly occurred under higher pollution level when sufficient gas precursors was transport to the level. The BrC may be also subject to bleaching process and lose the absorbance (Sareen et al., 2013; Lee et al., 2014; Wong et al., 2019), because the profiles in this study were conducted over an urban megacity where the sampled pollutants were fairly young and may have not experienced sufficient ageing for BrC to be degraded.

4. Conclusions

This study provides detailed characterization of vertical profiles of aerosol optical properties over the Beijing region by continuous aircraft in-situ measurements at different stages during the pollution events. The results combining the direct measurements of scattering and absorption at multiple wavelength, give a full picture of how the optical properties had evolved at different layers during typical pollution event.

During clean period for pollution initialization (CP), the aerosols showed relatively uniform characteristics throughout the planetary boundary layer (PBL) and lower free troposphere (FT), such as lowing scattering or absorption coefficient, larger SAE (due to smaller particle size) and lower fraction of brown carbon (BrC) reflected by smaller AAE. The transition period (TP) when pollution was developing had large variation of all optical properties, and enhanced aerosol loadings at higher altitude were encountered when being influenced by regional advection. The fully developed heavy pollution period (HP) featured with the shallow PBL accumulated over 80 % of the scattering and absorption within the PBL, and deceased SAE due to enlarged particles size. Notably the absorption towards shorter wavelength became larger under more polluted environment, especially for the higher altitude.

The AOD and AAOD measured by passive remote sensing was for the first time compared with in-situ measurements over this polluted region. AOD showed high correlation between AERONET and in-situ measurement within 10 %, and the most discrepancy between both could be possibly resolved by considering the hygroscopic growth of aerosols under high RH condition. The AAOD however showed 10-25 % higher for remote sensing especially at shorter wavelength, consistent with other studies(Müller et al., 2012;Andrews et al., 2017). The possibilities of causing this could be the non-homogeneously vertically structure of optical properties, mixing state of light-absorbing aerosol, and also the particle hygroscopic growth, which are unable to be ruled out only using the results here.

BC was the main heating species, ~~having~~ 0.05 K/h, 0.1 K/h and 0.15 K/h heating rate at local time 12:00 to 15:00 in the PBL during pollution initialization, transition and full development respectively, ~~and~~ showed positive vertical gradient ~~of heating~~ during regional transport period when pollution was advected at high level from the polluted ~~south~~ region ~~outside~~ of Beijing (Tian et al., 2019). The contribution of BrC to heating rate was found to increase by 20 % throughout the column from CP to HP period, in particular the increased BrC contribution was pronounced at the layer above the PBL during HP, which was proposed to result from the intensive photochemical reactions above the PBL. The BrC present at this layer will have the potential to contribute to the heating at this layer, hence enhancing the temperature inversion on top of the PBL hereby the capping effect to the pollutants trapped in the PBL. Particles at higher altitude may be transported to wider region spatially in both vertical and horizontal directions through convection, which may lead BrC present at this layer to have wilder and longer radiative impacts.

Different mechanism of BrC formation at different levels such as above the PBL (where more solar flux received) or within the PBL (where more moisture was constrained) warrants future studies.

Data availability. All data in this paper are available from the authors upon request (tianping@bj.cma.gov.cn).

Competing interests. The authors declare no conflicts of interest.

Author contribution. D. D., and M. H., led and designed the study; P. T., and D. L., designed the study, set up the experiment, analyzed the data, and wrote the paper. P. T., D. Z., and Q. L., conducted the aircraft observation. C. Y., performed the radiative transfer model calculation. P. T., D. L., Z. D., L. R., and Y. W., contributed to the aircraft data analysis. S. D., and K. H., contribute to the surface data analysis. G. Z., and C. Z., conducted the aerosol absorption comparison experiment.

Acknowledgment. This research was supported by the National key Research and Development Program of China (2016YFA0602001), and the National Natural Science Foundation of China (41875044, 41675038, 41875167). Part of this work is supported by the National Center of Meteorology, Abu Dhabi, UAE under the UAE Research Program for Rain Enhancement Science.

Reference

Anderson, T. L., and Ogren, J. A.: Determining Aerosol Radiative Properties Using the TSI 3563 Integrating Nephelometer, Aerosol Sci. Technol., 29, 57-69, 10.1080/02786829808965551, 1998.

Andrews, E., Sheridan, P. J., Fiebig, M., McComiskey, A., Ogren, J. A., Arnott, P., Covert, D., Elleman, R., Gasparini, R., Collins, D., Jonsson, H., Schmid, B., and Wang, J.: Comparison of methods for deriving aerosol asymmetry parameter, J. Geophys. Res., 111, 10.1029/2004jd005734, 2006.

Andrews, E., Sheridan, P. J., and Ogren, J. A.: Seasonal differences in the vertical profiles of aerosol optical properties over rural Oklahoma, Atmos. Chem. Phys., 11, 10661-10676, 10.5194/acp-11-10661-2011, 2011.

Andrews, E., Ogren, J. A., Kinne, S., and Samset, B.: Comparison of AOD, AAOD and column single scattering albedo from AERONET retrievals and in situ profiling measurements, Atmos. Chem. Phys., 17, 6041-6072, 10.5194/acp-17-6041-2017, 2017.

Arnott, W. P., Hamasha, K., Moosmüller, H., Sheridan, P. J., and Ogren, J. A.: Towards Aerosol Light-Absorption Measurements with a 7-Wavelength Aethalometer: Evaluation with a Photoacoustic Instrument and 3-Wavelength Nephelometer, Aerosol Sci. Technol., 39, 17-29, 10.1080/027868290901972, 2005.

Ban-Weiss, G. A., Cao, L., Bala, G., and Caldeira, K.: Dependence of climate forcing and response on the altitude of black carbon aerosols, Clim. Dynam., 38, 897-911, 10.1007/s00382-011-1052-y, 2011.

Bergin, M. H., Cass, G. R., Xu, J., Fang, C., Zeng, L. M., Yu, T., Salmon, L. G., Kiang, C. S., Tang, X. Y., Zhang, Y. H., and Chameides, W. L.: Aerosol radiative, physical, and chemical properties in Beijing during June 1999, J. Geophys. Res., 106, 17969-17980, Doi 10.1029/2001jd900073, 2001.

Bond, T. C., Doherty, S. J., Fahey, D. W., Forster, P. M., Berntsen, T., DeAngelo, B. J., Flanner, M. G., Ghan, S., Kärcher, B., Koch, D., Kinne, S., Kondo, Y., Quinn, P. K., Sarofim, M. C., Schultz, M. G., Schulz, M., Venkataraman, C., Zhang, H., Zhang, S., Bellouin, N., Guttikunda, S. K., Hopke, P. K., Jacobson, M. Z., Kaiser, J. W., Klimont, Z., Lohmann, U., Schwarz, J. P., Shindell, D., Storelvmo, T., Warren, S. G., and Zender, C. S.: Bounding the role of black carbon in the climate system: A scientific assessment, J. Geophys. Res. Atmos., 118, 5380-5552, 10.1002/jgrd.50171, 2013.

Carrico, C. M., Rood, M. J., and Ogren, J. A.: Aerosol light scattering properties at Cape Grim, Tasmania,

during the First Aerosol Characterization Experiment (ACE 1), J. Geophys. Res., 103, 16565, 10.1029/98jd00685, 1998.

Cazorla, A., Bahadur, R., Suski, K. J., Cahill, J. F., Chand, D., Schmid, B., Ramanathan, V., and Prather, K. A.: Relating aerosol absorption due to soot, organic carbon, and dust to emission sources determined from in-situ chemical measurements, Atmos. Chem. Phys., 13, 9337-9350, 10.5194/acp-13-9337-2013, 2013.

Chakrabarty, R. K., Garro, M. A., Wilcox, E. M., and Moosmüller, H.: Strong radiative heating due to wintertime black carbon aerosols in the Brahmaputra River Valley, Geophys. Res. Lett., 39, n/a-n/a, 10.1029/2012gl051148, 2012.

Che, H., Zhang, X., Chen, H., Damiri, B., Goloub, P., Li, Z., Zhang, X., Wei, Y., Zhou, H., Dong, F., Li, D., and Zhou, T.: Instrument calibration and aerosol optical depth validation of the China Aerosol Remote Sensing Network, J. Geophys. Res., 114, 10.1029/2008jd011030, 2009.

Chen, Y., Zhao, C., Zhang, Q., Deng, Z., Huang, M., and Ma, X.: Aircraft study of Mountain Chimney Effect of Beijing, China, J. Geophys. Res., 114, 10.1029/2008jd010610, 2009.

Chung, C. E., Ramanathan, V., and Decremer, D.: Observationally constrained estimates of carbonaceous aerosol radiatice forcing, PNAS, 109, 5, 10.1073/pnas.1203707109/-/DCSupplemental, 2012.

Ding, A. J., Huang, X., Nie, W., Sun, J. N., Kerminen, V. M., Petäjä, T., Su, H., Cheng, Y. F., Yang, X. Q., Wang, M. H., Chi, X. G., Wang, J. P., Virkkula, A., Guo, W. D., Yuan, J., Wang, S. Y., Zhang, R. J., Wu, Y. F., Song, Y., Zhu, T., Zilitinkevich, S., Kulmala, M., and Fu, C. B.: Enhanced haze pollution by black carbon in megacities in China, Geophys. Res. Lett., 43, 2873-2879, 10.1002/2016gl067745, 2016.

Drinovec, L., Gregorič, A., Zotter, P., Wolf, R., Bruns, E. A., Prévôt, A. S. H., Petit, J.-E., Favez, O., Sciare, J., Arnold, I. J., Chakrabarty, R. K., Moosmüller, H., Filep, A., and Močnik, G.: The filter-loading effect by ambient aerosols in filter absorption photometers depends on the coating of the sampled particles, Atmos. Meas. Tech., 10, 1043-1059, 10.5194/amt-10-1043-2017, 2017.

Ebert, M., Weinbruch, S., Rausch, A., Gorzawski, G., Helas, G., Hoffmann, P., and Wex, H.: Complex refractive index of aerosols during LACE 98 as derived from the analysis of individual particles, J. Geophys. Res. Atmos., 107, LAC 3-1-LAC 3-15, 10.1029/2000jd000195, 2002.

Emde, C., Buras-Schnell, R., Kylling, A., Mayer, B., Gasteiger, J., Hamann, U., Kylling, J., Richter, B.,

Pause, C., Dowling, T., and Bugliaro, L.: The libRadtran software package for radiative transfer calculations (version 2.0.1), Geosci. Model Dev., 9, 1647-1672, 10.5194/gmd-9-1647-2016, 2016.
Ervens, B., Turpin, B. J., and Weber, R. J.: Secondary organic aerosol formation in cloud droplets and aqueous particles (aqSOA): a review of laboratory, field and model studies, Atmos. Chem. Phys., 11, 11069-11102, 10.5194/acp-11-11069-2011, 2011.
Feng, Y., Ramanathan, V., and Kotamarthi, V. R.: Brown carbon: a significant atmospheric absorber of solar radiation?, Atmos. Chem. Phys., 13, 8607-8621, 10.5194/acp-13-8607-2013, 2013.
Ferrero, L., Castelli, M., Ferrini, B. S., Moscatelli, M., Perrone, M. G., Sangiorgi, G., amp, apos, Angelo, L., Rovelli, G., Moroni, B., Scardazza, F., Močnik, G., Bolzacchini, E., Petitta, M., and Cappelletti, D.: Impact of black carbon aerosol over Italian basin valleys: high-resolution measurements along vertical profiles, radiative forcing and heating rate, Atmos. Chem. Phys., 14, 9641-9664, 10.5194/acp-14-9641-2014, 2014.
Ferrero, L., Mocnik, G., Cogliati, S., Gregoric, A., Colombo, R., and Bolzacchini, E.: Heating Rate of Light Absorbing Aerosols: Time-Resolved Measurements, the Role of Clouds, and Source Identification, Environ Sci Technol, 52, 3546-3555, 10.1021/acs.est.7b04320, 2018.
Gao, R. S., Hall, S. R., Swartz, W. H., Schwarz, J. P., Spackman, J. R., Watts, L. A., Fahey, D. W., Aikin, K. C., Shetter, R. E., and Bui, T. P.: Calculations of solar shortwave heating rates due to black carbon and ozone absorption using in situ measurements, J. Geophys. Res., 113, 10.1029/2007jd009358, 2008.
Gyawali, M., Arnott, W. P., and Moosmuller, H.: In situ aerosol optics in Reno, NV, USA, during and after the summer 2008 California wildfires and the influence of absorbing and non-absorbing organic coatings on spectral light absorption, Atmos. Chem. Phys., 9, 8009-8015, 2009.
Hansen, A. D. A.: The Aethalometer Manual, Berkeley, California, USA, pp., 2005.
Haywood, J. M., Schwarzkopf, M. D., and Ramaswamy, V.: Estimates of radiative forcing due to modeled increases in tropospheric ozone, J. Geophys. Res. Atmos., 103, 16999-17007, 10.1029/98jd01348, 1998.
He, X., Li, C. C., Lau, A. K. H., Deng, Z. Z., Mao, J. T., Wang, M. H., and Liu, X. Y.: An intensive study of aerosol optical properties in Beijing urban area, Atmos. Chem. Phys., 9, 8903-8915, 2009.
Hodnebrog, O., Myhre, G., and Samset, B. H.: How shorter black carbon lifetime alters its climate effect, Nat. Commun., 5, 1-7, 10.1038/ncomms6065, 2014.

566 Jing, J. S., Zhang, R. J., Tao, J., and Zhang, L. M.: Observations of Aerosol Optical Properties in the
567 Beijing Urban Area inSummer, Atmos. Sci. Lett., 4, 338-343, 2011.
568 Kedia, S., Ramachandran, S., Kumar, A., and Sarin, M. M.: Spatiotemporal gradients in aerosol radiative
569 forcing and heating rate over Bay of Bengal and Arabian Sea derived on the basis of optical, physical,
570 and chemical properties, J. Geophys. Res., 115, 10.1029/2009jd013136, 2010.
571 Kirchstetter, T. W., Novakov, T., and Hobbs, P. V.: Evidence that the spectral dependence of light
572 absorption by aerosols is affected by organic carbon, J. Geophys. Res. Atmos., 109, n/a-n/a,
573 10.1029/2004jd004999, 2004.
574 Klingmüller, K., Lelieveld, J., Karydis, V. A., and Stenchikov, G. L.: Direct radiative effect of dust–
575 pollution interactions, Atmos. Chem. Phys., 19, 7397-7408, 10.5194/acp-19-7397-2019, 2019.
576 Koch, D., and Del Genio, A. D.: Black carbon semi-direct effects on cloud cover: review and synthesis,
577 Atmos. Chem. Phys., 10, 7685-7696, 10.5194/acp-10-7685-2010, 2010.
578 Lack, D. A., and Cappa, C. D.: Impact of brown and clear carbon on light absorption enhancement, single
579 scatter albedo and absorption wavelength dependence of black carbon, Atmos. Chem. Phys., 10, 4207-
580 4220, 10.5194/acp-10-4207-2010, 2010.
581 Lack, D. A., Bahreni, R., Langridge, J. M., Gilman, J. B., and Middlebrook, A. M.: Brown carbon
582 absorption linked to organic mass tracers in biomass burning particles, Atmos. Chem. Phys., 13, 2415-
583 2422, 10.5194/acp-13-2415-2013, 2013.
584 Laskin, A., Laskin, J., and Nizkorodov, S. A.: Chemistry of atmospheric brown carbon, Chemical reviews,
585 115, 4335-4382, 10.1021/cr5006167, 2015.
586 Lee, H. J., Aiona, P. K., Laskin, A., Laskin, J., and Nizkorodov, S. A.: Effect of solar radiation on the
587 optical properties and molecular composition of laboratory proxies of atmospheric brown carbon, Environ.
588 Sci. Technol., 48, 10217-10226, 10.1021/es502515r, 2014.
589 Li, Z., Guo, J., Ding, A., Liao, H., Liu, J., Sun, Y., Wang, T., Xue, H., Zhang, H., and Zhu, B.: Aerosol
590 and boundary-layer interactions and impact on air quality, National Science Review, 4, 810-833,
591 10.1093/nsr/nwx117, 2017.
592 Liao, H., and Seinfeld, J. H.: Radiative forcing by mineral dust aerosols: Sensitivity to key variables, J.
593 Geophys. Res. Atmos., 103, 31637-31645, 10.1029/1998jd200036, 1998.

Liu, D., Taylor, J. W., Young, D. E., Flynn, M. J., Coe, H., and Allan, J. D.: The effect of complex black carbon microphysics on the determination of the optical properties of brown carbon, Geophys. Res. Lett., 42, 613-619, 10.1002/2014gl062443, 2015a.

Liu, J., Scheuer, E., Dibb, J., Diskin, G. S., Ziemba, L. D., Thornhill, K. L., Anderson, B. E., Wisthaler, A., Mikoviny, T., Devi, J. J., Bergin, M., Perring, A. E., Markovic, M. Z., Schwarz, J. P., Campuzano-Jost, P., Day, D. A., Jimenez, J. L., and Weber, R. J.: Brown carbon aerosol in the North American continental troposphere: sources, abundance, and radiative forcing, Atmos. Chem. Phys., 15, 7841-7858, 10.5194/acp-15-7841-2015, 2015b.

Liu, P., Zhao, C., Liu, P., Deng, Z., Huang, M., Ma, X., and Tie, X.: Aircraft study of aerosol vertical distributions over Beijing and their optical properties, Tellus B: Chemical and Physical Meteorology, 61, 756-767, 10.1111/j.1600-0889.2009.00440.x, 2009.

Müller, D., Lee, K. H., Gasteiger, J., Tesche, M., Weinzierl, B., Kandler, K., Müller, T., Toledano, C., Otto, S., Althausen, D., and Ansmann, A.: Comparison of optical and microphysical properties of pure Saharan mineral dust observed with AERONET Sun photometer, Raman lidar, and in situ instruments during SAMUM 2006, J. Geophys. Res. Atmos., 117, n/a-n/a, 10.1029/2011jd016825, 2012.

Müller, T., Nowak, A., Wiedensohler, A., Sheridan, P., Laborde, M., Covert, D. S., Marinoni, A., Imre, K., Henzing, B., Roger, J.-C., dos Santos, S. M., Wilhelm, R., Wang, Y.-Q., and de Leeuw, G.: Angular Illumination and Truncation of Three Different Integrating Nephelometers: Implications for Empirical, Size-Based Corrections, Aerosol Sci. Technol., 43, 581-586, 10.1080/02786820902798484, 2009.

Mallet, M., Pont, V., Liousse, C., Gomes, L., Pelon, J., Osborne, S., Haywood, J., Roger, J. C., Dubuisson, P., Mariscal, A., Thouret, V., and Goloub, P.: Aerosol direct radiative forcing over Djougou (northern Benin) during the African Monsoon Multidisciplinary Analysis dry season experiment (Special Observation Period-0), J. Geophys. Res., 113, 10.1029/2007jd009419, 2008.

Massabò, D., Caponi, L., Bernardoni, V., Bove, M. C., Brotto, P., Calzolai, G., Cassola, F., Chiari, M., Fedi, M. E., Fermo, P., Giannoni, M., Lucarelli, F., Nava, S., Piazzalunga, A., Valli, G., Vecchi, R., and Prati, P.: Multi-wavelength optical determination of black and brown carbon in atmospheric aerosols, Atmos. Environ., 108, 1-12, 10.1016/j.atmosenv.2015.02.058, 2015.

Nakayama, T., Sato, K., Matsumi, Y., Imamura, T., Yamazaki, A., and Uchiyama, A.: Wavelength and

NOx dependent complex refractive index of SOAs generated from the photooxidation of toluene, Atmos. Chem. Phys., 13, 531-545, 10.5194/acp-13-531-2013, 2013.
Nazarenko, L., Rind, D., Tsigaridis, K., Del Genio, A. D., Kelley, M., and Tausnev, N.: Interactive nature of climate change and aerosol forcing, J. Geophys. Res. Atmos., 122, 3457-3480, 10.1002/2016jd025809, 2017.
Nguyen, T. B., Lee, P. B., Updyke, K. M., Bones, D. L., Laskin, J., Laskin, A., and Nizkorodov, S. A.: Formation of nitrogen- and sulfur-containing light-absorbing compounds accelerated by evaporation of water from secondary organic aerosols, J. Geophys. Res. Atmos., 117, n/a-n/a, 10.1029/2011jd016944, 2012.
Petaja, T., Jarvi, L., Kerminen, V. M., Ding, A. J., Sun, J. N., Nie, W., Kujansuu, J., Virkkula, A., Yang, X. Q., Fu, C. B., Zilitinkevich, S., and Kulmala, M.: Enhanced air pollution via aerosol-boundary layer feedback in China, Sci. Repts., 6, 18998, 10.1038/srep18998, 2016.
Petra Seibert, F. B., Sven-Erik Gryning, Sylvain Joffre, Alix Rasmussen, Philippe Tercier: Review and intercomparison of operational methods for the determination of the mixing height, Atmos. Environ., 34, 27, 2000.
Quinn, P. K.: Aerosol optical properties during INDOEX 1999: Means, variability, and controlling factors, J. Geophys. Res., 107, 10.1029/2000jd000037, 2002.
Ramachandran, S., and Kedia, S.: Black carbon aerosols over an urban region: Radiative forcing and climate impact, J. Geophys. Res., 115, 10.1029/2009jd013560, 2010.
Ramana, M. V., Ramanathan, V., Kim, D., Roberts, G. C., and Corrigan, C. E.: Albedo, atmospheric solar absorption and heating rate measurements with stacked UAVs, Quarterly Journal of the Royal Meteorological Society, 133, 1913-1931, 10.1002/qj.172, 2007.
Ramana, M. V., Ramanathan, V., Feng, Y., Yoon, S. C., Kim, S. W., Carmichael, G. R., and Schauer, J. J.: Warming influenced by the ratio of black carbon to sulphate and the black-carbon source, Nature Geoscience, 3, 542-545, 10.1038/ngeo918, 2010.
Ramanathan, V., Crutzen, P. J., Kiehl, J. T., and Rosenfeld, D.: Aerosols, climate, and the hydrological cycle, Science, 294, 2119-2124, 10.1126/science.1064034, 2001.
Ran, L., Deng, Z., Xu, X., Yan, P., Lin, W., Wang, Y., Tian, P., Wang, P., Pan, W., and Lu, D.: Vertical

650 profiles of black carbon measured by a micro-aethalometer in summer in the North China Plain, Atmos.
651 Chem. Phys., 16, 10441-10454, 10.5194/acp-16-10441-2016, 2016a.
652 Ran, L., Deng, Z. Z., Wang, P. C., and Xia, X. A.: Black carbon and wavelength-dependent aerosol
653 absorption in the North China Plain based on two-year aethalometer measurements, Atmos. Environ., 142,
654 132-144, 10.1016/j.atmosenv.2016.07.014, 2016b.
655 Rosati, B., Herrmann, E., Bucci, S., Fierli, F., Cairo, F., Gysel, M., Tillmann, R., Größ, J., Gobbi, G. P.,
656 Di Liberto, L., Di Donfrancesco, G., Wiedensohler, A., Weingartner, E., Virtanen, A., Mentel, T. F., and
657 Baltensperger, U.: Studying the vertical aerosol extinction coefficient by comparing in situ airborne data
658 and elastic backscatter lidar, Atmos. Chem. Phys., 16, 4539-4554, 10.5194/acp-16-4539-2016, 2016.
659 Sühring, M., Maronga, B., Herbort, F., and Raasch, S.: On the Effect of Surface Heat-Flux Heterogeneities
660 on the Mixed-Layer-Top Entrainment, Boundary-Layer Meteorol., 151, 531-556, 10.1007/s10546-014-
661 9913-7, 2014.
662 Sahu, L. K., Kondo, Y., Moteki, N., Takegawa, N., Zhao, Y., Cubison, M. J., Jimenez, J. L., Vay, S., Diskin,
663 G. S., Wisthaler, A., Mikoviny, T., Huey, L. G., Weinheimer, A. J., and Knapp, D. J.: Emission
664 characteristics of black carbon in anthropogenic and biomass burning plumes over California during
665 ARCTAS-CARB 2008, J. Geophys. Res. Atmos., 117, n/a-n/a, 10.1029/2011jd017401, 2012.
666 Saleh, R., Marks, M., Heo, J., Adams, P. J., Donahue, N. M., and Robinson, A. L.: Contributon of brown
667 carbon and lensing to the direct radiative effect of carbonaceous aerosols from biomass and biofuel
668 burning emissions, J. Geophys. Res., 120, 10285-10296, 10.1002/, 2015.
669 Sareen, N., Moussa, S. G., and McNeill, V. F.: Photochemical aging of light-absorbing secondary organic
670 aerosol material, The journal of physical chemistry. A, 117, 2987-2996, 10.1021/jp309413j, 2013.
671 Schnaiter, M., Schmid, O., Petzold, A., Fritzsche, L., Klein, K. F., Andreae, M. O., Helas, G., Thielmann,
672 A., Gimmler, M., Möhler, O., Linke, C., and Schurath, U.: Measurement of Wavelength-Resolved Light
673 Absorption by Aerosols Utilizing a UV-VIS Extinction Cell, Aerosol Sci. Technol., 39, 249-260,
674 10.1080/027868290925958, 2005.
675 Shamjad, P. M., Tripathi, S. N., Pathak, R., Hallquist, M., Arola, A., and Bergin, M. H.: Contribution of
676 Brown Carbon to Direct Radiative Forcing over the Indo-Gangetic Plain, Environ Sci Technol, 49, 10474-
677 10481, 10.1021/acs.est.5b03368, 2015.

Su, T., Li, J., Li, C., Xiang, P., Lau, A. K.-H., Guo, J., Yang, D., and Miao, Y.: An intercomparison of long-term planetary boundary layer heights retrieved from CALIPSO, ground-based lidar, and radiosonde measurements over Hong Kong, J. Geophys. Res. Atmos., 122, 3929-3943, 10.1002/2016jd025937, 2017.

Sun, J., Zhi, G., Hitzenberger, R., Chen, Y., Tian, C., Zhang, Y., Feng, Y., Cheng, M., Zhang, Y., Cai, J., Chen, F., Qiu, Y., Jiang, Z., Li, J., Zhang, G., and Mo, Y.: Emission factors and light absorption properties of brown carbon from household coal combustion in China, Atmos. Chem. Phys., 17, 4769-4780, 10.5194/acp-17-4769-2017, 2017.

Tian, P., Liu, D., Huang, M., Liu, Q., Zhao, D., Ran, L., Deng, Z., Wu, Y., Fu, S., Bi, K., Gao, Q., He, H., Xue, H., and Ding, D.: The evolution of an aerosol event observed from aircraft in Beijing: An insight into regional pollution transport, Atmos. Environ., 206, 11-20, 10.1016/j.atmosenv.2019.02.005, 2019.

Torres, B., Dubovik, O., Toledano, C., Berjon, A., Cachorro, V. E., Lapyonok, T., Litvinov, P., and Goloub, P.: Sensitivity of aerosol retrieval to geometrical configuration of ground-based sun/sky radiometer observations, Atmos. Chem. Phys., 14, 847-875, 10.5194/acp-14-847-2014, 2014.

Tripathi, S. N., Srivastava, A. K., Dey, S., Satheesh, S. K., and Krishnamoorthy, K.: The vertical profile of atmospheric heating rate of black carbon aerosols at Kanpur in northern India, Atmos. Environ., 41, 6909-6915, 10.1016/j.atmosenv.2007.06.032, 2007.

Updyke, K. M., Nguyen, T. B., and Nizkorodov, S. A.: Formation of brown carbon via reactions of ammonia with secondary organic aerosols from biogenic and anthropogenic precursors, Atmos. Environ., 63, 22-31, 10.1016/j.atmosenv.2012.09.012, 2012.

Wang, F., Li, Z., Ren, X., Jiang, Q., He, H., Dickerson, R. R., Dong, X., and Lv, F.: Vertical distributions of aerosol optical properties during the spring 2016 ARIAs airborne campaign in the North China Plain, Atmos. Chem. Phys., 18, 8995-9010, 10.5194/acp-18-8995-2018, 2018a.

Wang, J., Nie, W., Cheng, Y., Shen, Y., Chi, X., Wang, J., Huang, X., Xie, Y., Sun, P., Xu, Z., Qi, X., Su, H., and Ding, A.: Light absorption of brown carbon in eastern China based on 3-year multi-wavelength aerosol optical property observations and an improved absorption Ångström exponent segregation method, Atmos. Chem. Phys., 18, 9061-9074, 10.5194/acp-18-9061-2018, 2018b.

Wang, Y., Che, H., Ma, J., Wang, Q., Shi, G., Chen, H., Goloub, P., and Hao, X.: Aerosol radiative forcing under clear, hazy, foggy, and dusty weather conditions over Beijing, China, Geophys. Res. Lett., 36,

706 10.1029/2009gl037181, 2009.
707 Wang, Z., Huang, X., and Ding, A.: Dome effect of black carbon and its key influencing factors: a one-
708 dimensional modelling study, Atmos. Chem. Phys., 18, 2821-2834, 10.5194/acp-18-2821-2018, 2018c.
709 Wilcox, E. M., Thomas, R. M., Praveen, P. S., Pistone, K., Bender, F. A., and Ramanathan, V.: Black
710 carbon solar absorption suppresses turbulence in the atmospheric boundary layer, Proc. Natl. Acad. Sci.
711 USA., 113, 11794-11799, 10.1073/pnas.1525746113, 2016.
712 Wong, J. P. S., Tsagkaraki, M., Tsiodra, I., Mihalopoulos, N., Violaki, K., Kanakidou, M., Sciare, J., Nenes,
713 A., and Weber, R. J.: Atmospheric evolution of molecular-weight-separated brown carbon from biomass
714 burning, Atmos. Chem. Phys., 19, 7319-7334, 10.5194/acp-19-7319-2019, 2019.
715 Wu, Y., Wang, X., Tao, J., Huang, R., Tian, P., Cao, J., Zhang, L., Ho, K.-F., Han, Z., and Zhang, R.: Size
716 distribution and source of black carbon aerosol in urban Beijing during winter haze episodes, Atmos.
717 Chem. Phys., 17, 7965-7975, 10.5194/acp-17-7965-2017, 2017.
718 Xia, X., Eck, T. F., Holben, B. N., Phillippe, G., and Chen, H.: Analysis of the weekly cycle of aerosol
719 optical depth using AERONET and MODIS data, J. Geophys. Res., 113, 10.1029/2007jd009604, 2008.
720 Xie, C., Xu, W., Wang, J., Wang, Q., Liu, D., Tang, G., Chen, P., Du, W., Zhao, J., Zhang, Y., Zhou, W.,
721 Han, T., Bian, Q., Li, J., Fu, P., Wang, Z., Ge, X., Allan, J., Coe, H., and Sun, Y.: Vertical characterization
722 of aerosol optical properties and brown carbon in winter in urban Beijing, China, Atmos. Chem. Phys.,
723 19, 165-179, 10.5194/acp-19-165-2019, 2019.
724 Yu, H., Liu, S. C., and Dickinson, R. E.: Radiative effects of aerosols on the evolution of the atmospheric
725 boundary layer, J. Geophys. Res., 107, 10.1029/2001jd000754, 2002.
726 Yu, P. F., Toon, O. B., Bardeen, C. G., Zhu, Y. Q., Rosenlof, K. H., Portmann, R. W., Thornberry, T. D.,
727 Gao, R. S., SDavis, S. M., Wolf, E. T., Gouw, J. D., Peterson, D. A., Fromm, M. D., and Robock, A.:
728 Black carbon lofts wildfire smoke high into the stratosphere to form a persistent plume, Science, 365, 14,
729 2019.
730 Zhang, R., Jing, J., Tao, J., Hsu, S. C., Wang, G., Cao, J., Lee, C. S. L., Zhu, L., Chen, Z., Zhao, Y., and
731 Shen, Z.: Chemical characterization and source apportionment of PM2.5 in Beijing: seasonal perspective,
732 Atmos. Chem. Phys., 13, 7053-7074, 10.5194/acp-13-7053-2013, 2013.
733 Zhang, X. Y., Wang, J. Z., Wang, Y. Q., Liu, H. L., Sun, J. Y., and Zhang, Y. M.: Changes in chemical

components of aerosol particles in different haze regions in China from 2006 to 2013 and contribution of meteorological factors, Atmos. Chem. Phys., 15, 12935-12952, 10.5194/acp-15-12935-2015, 2015.
Zhang, Y., Forrister, H., Liu, J., Dibb, J., Anderson, B., Schwarz, J. P., Perring, A. E., Jimenez, J. L., Campuzano-Jost, P., Wang, Y., Nenes, A., and Weber, R. J.: Top-of-atmosphere radiative forcing affected by brown carbon in the upper troposphere, Nature Geoscience, 10.1038/ngeo2960, 2017.
Zhao, D. L., Huang, M. Y., Tian, P., He, H., Lowe, D., Zhou, W., Sheng, J. J., Wang, F., Bi, K., Kong, S. F., Yang, Y., Liu, Q., Liu, D. T., and Ding, D. P.: Vertical characteristics of black carbon physical properties over Beijing region in warm and cold seasons, Atmos. Environ., 213, 296-310, 2019a.
Zhao, G., Zhao, C. S., Kung, Y., Bian, Y. X., Tao, J. C., Shen, C. Y., and Yu, Y. L.: Calculating the aerosol asymmetry factor based on measurements from the humidified nephelometer system, Atmos. Chem. Phys., 18, 9049-9060, 10.5194/acp-18-9049-2018, 2018.
Zhao, P. S., Ding, J., Du, X., and Su, J.: High time-resolution measurement of light scattering hygroscopic growth factor in Beijing A novel method for high relative humidity conditions, Atmos. Environ., 215, 10.1016/j.atmosenv.2019.116912, 2019b.
Zhao, R., Lee, A. K. Y., Huang, L., Li, X., Yang, F., and Abbatt, J. P. D.: Photochemical processing of aqueous atmospheric brown carbon, Atmos. Chem. Phys., 15, 6087-6100, 10.5194/acp-15-6087-2015, 2015.
Zhong, J., Zhang, X., Dong, Y., Wang, Y., Liu, C., Wang, J., Zhang, Y., and Che, H.: Feedback effects of boundary-layer meteorological factors on cumulative explosive growth of PM_{2.5} during winter heavy pollution episodes in Beijing from 2013 to 2016, Atmos. Chem. Phys., 18, 247-258, 10.5194/acp-18-247-2018, 2018.

Table 1. Flight summary in this study.

Flight number	Time range Local time	Case	Pollution period	Mixing layer height
RF1	20161115 12:00	Case_1	LP	1450 m
RF2	20161115 14:00	Case_1	LP	1450 m
RF3	20161116 12:00	Case_1	TP	850 m
RF4	20161116 14:00	Case_1	TP	750 m
RF5	20161117 12:00	Case_1	TP(Cloud)	1250 m
RF6	20161117 14:00	Case_1	TP(Cloud)	1150 m
RF7	20161118 12:00	Case_1	HP(Cloud)	1050 m
RF8	20161210 14:00	Case_2	LP	950 m
RF9	20161211 14:00	Case_2	MP	950 m
RF10	20161212 14:00	Case_2	HP	450 m
RF11	20161216 14:00	Case_3	TP	350 m
RF12	20161217 14:00	Case_3	HP	350 m
RF13	20161218 14:00	Case_3	HP	350 m
RF14	20161219 14:00	Case_3	HP	250 m

[1] LP, TP, and HP represents the low, transition and high pollution period during a pollution event.

Table 2. Summary of input parameters for the radiative transfer calculation using Discrete Ordinates Radiative Transfer Code (DISORT)

Parameter	Input value
Radiative transfer solver	DISORT, 12-streams, delta-m method
Gas absorption parameterization	LOWTRAN/SBDART parameterization
Wavelength range	250-2550nm
Atmosphere	Standard Mid-latitude atmosphere
Aerosol	The 25 layers from the surface to 5000 m was chosen inside the DISORT, and every 200 m average aerosol optical properties at 550 nm was used; AOD values are derived from in-situ Aurora3000 and AE33 measurements, also applying an exponential λ-dependent function SSA values are from in-situ σ_{sca} and σ_{abs} measurement SAE values are from in-situ Aurora3000 measurement AAE values are from in-situ AE33 measurement Asymmetry factor (g) is derived from the Aurora3000 measurement and uses Henyey-Greenstein phase function
Location	39.54ºN, 116.23ºE
Time	Flight time
Solar zenith angle	Effective solar zenith angle Using local time and aircraft location
Surface albedo	IGBP surface type 13 (Urban)

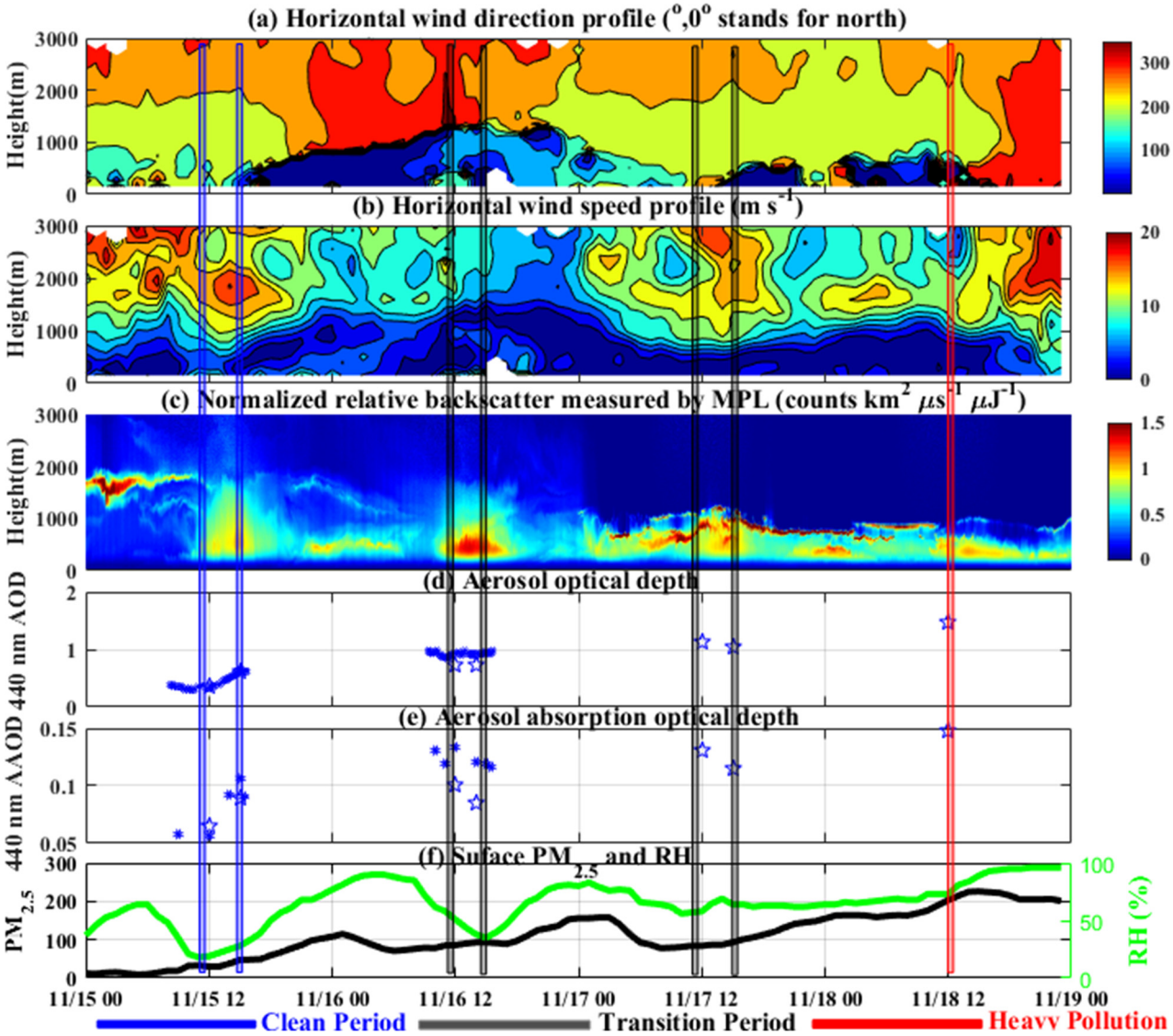

Fig. 1. Temporal variations from Nov. 15th to 18th of vertical profiles of wind direction (a), and wind speed (b) measured by wind profile radar,; (c) particle extinction measured by MPL lidar;) aerosol optical depth (d) and aerosol absorption optical depth (e) from AERONET (asterisk) and derived from aircraft in-situ measurements (open star)(f) surface $PM_{2.5}$ and RH.). The vertical bars denote the periods of flight profiles, with blue, black and red representing the clean period, transition period and heavy pollution during a pollution event respectively. The other two pollution events ~~can refer to~~ supplement

Fig. S2 and Fig. S3.

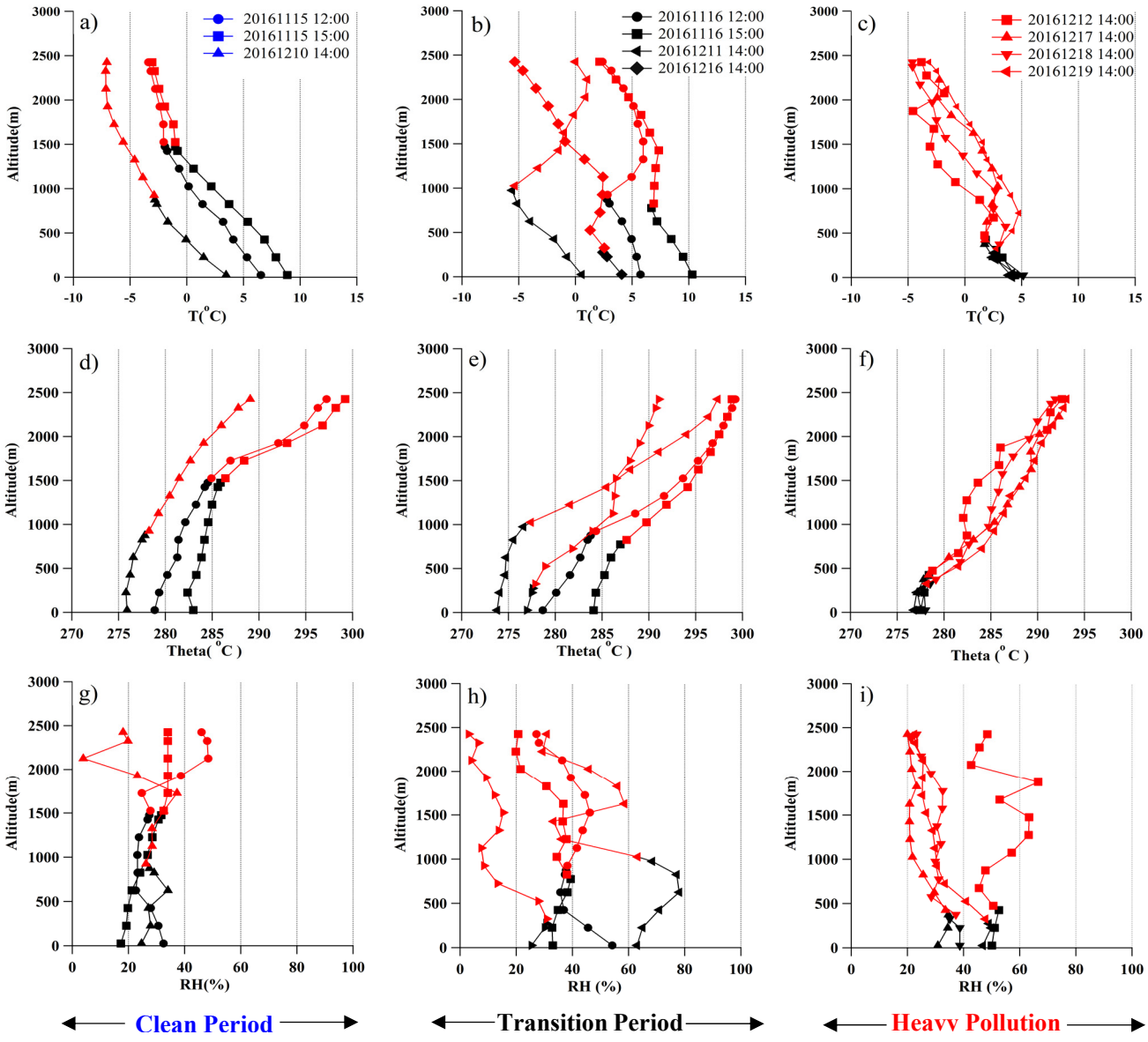

Fig. 2. Vertical profiles of temperature (a, b, c), relative humidity (d, e, f) and potential temperature (g, h, i) for Clean Period, Transition Period and Heavy Pollution period, respectively. The black and red dots represent for inside the PBL and above the PBL.

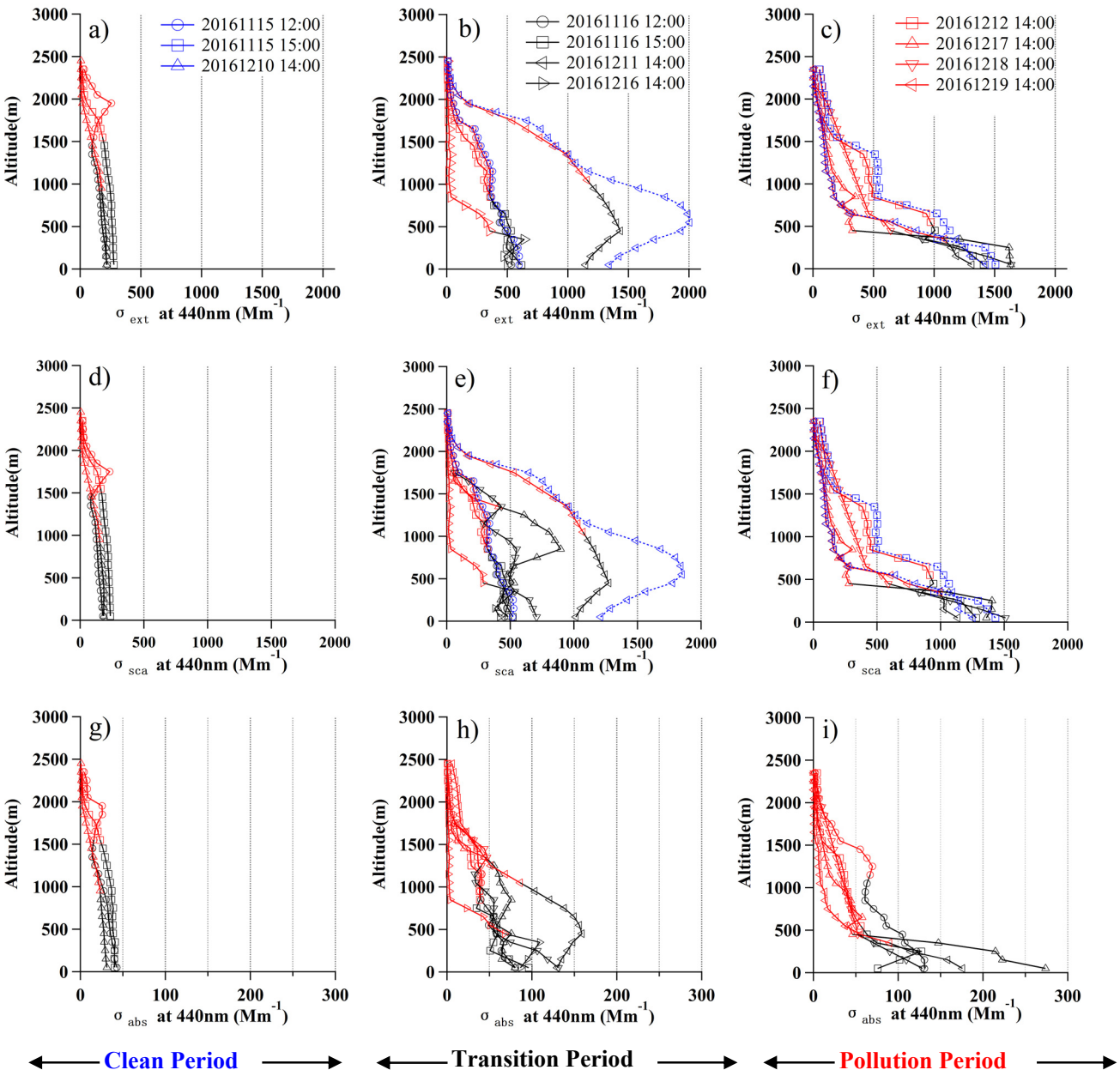

Fig. 3. Vertical profiles of aerosol extinction, scattering and absorption coefficient at 440 nm for CP (blue), TP (black) and HP period (red), respectively. The black and red lines represent for inside and above the ML, respectively. The hygroscopic-corrected profiles ~~was~~ shown ~~in~~ blue lines.

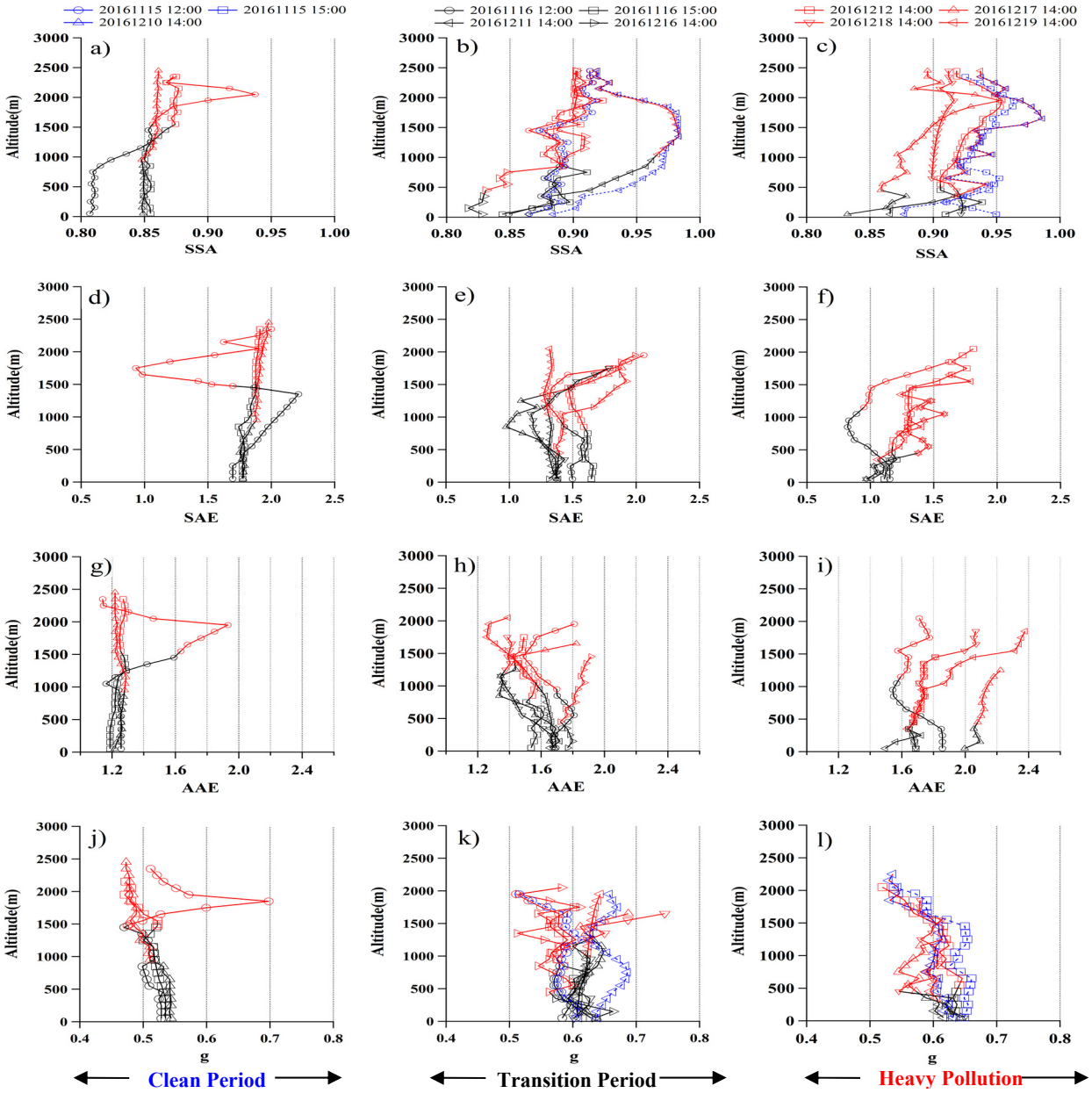

Fig. 4. Vertical profiles of aerosol single scattering albedo at 440 nm (SSA, a - c), scattering Angström exponent (SAE, d - f), absorption Angström exponent (AAE, g - i), and asymmetry parameter (g, j - l) for CP (left panel), TP (middle panel) and HP period (right panel), respectively. The hygroscopicity

corrected profiles was shown in blue lines.

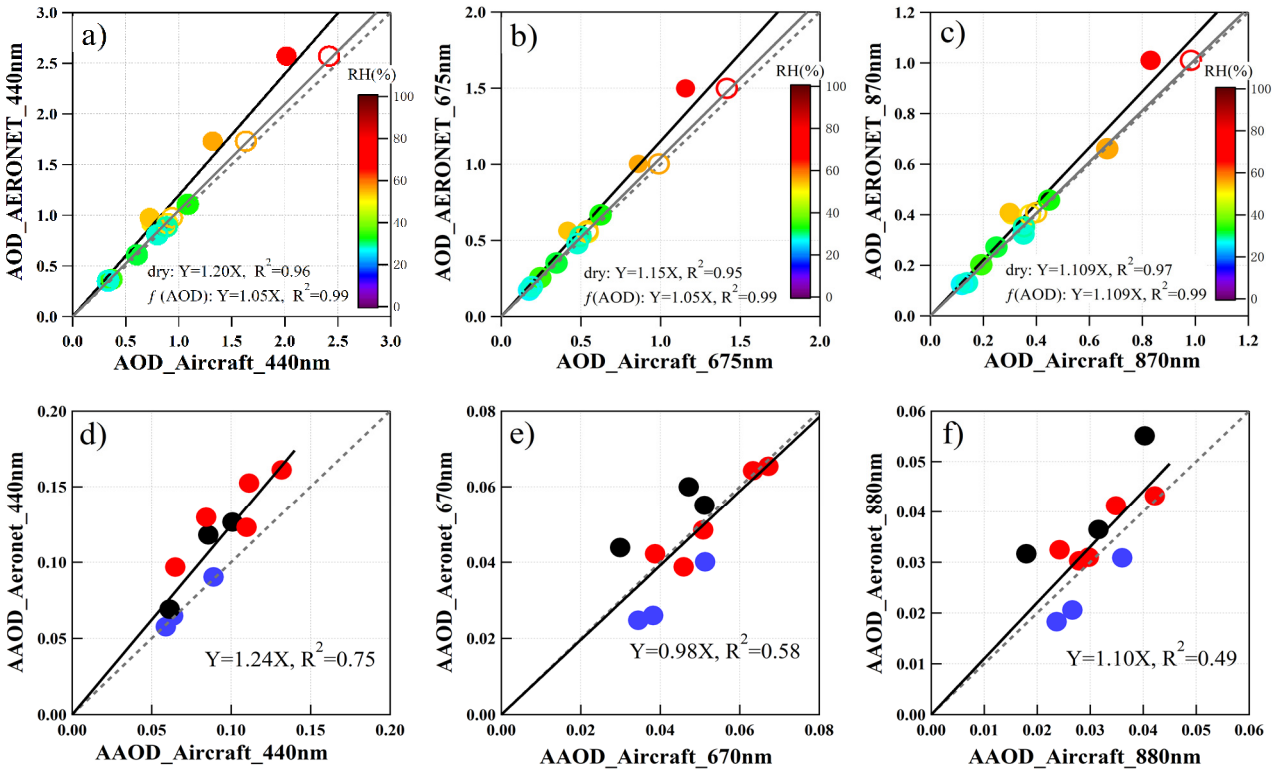

Fig. 5. Comparison between AERONET and aircraft in-situ constrained AOD and AAOD: a) - c) The comparison of AOD at 440nm, 675nm, and 870nm colored by RH; the solid and open markers denote the dry and hygroscopicity-corrected condition; d) – f) Comparison of AAOD at 440nm, 670nm, and 880nm. The blue, black, and red ~~nots~~ represent ~~for~~ CP, TP, and HP period, respectively.

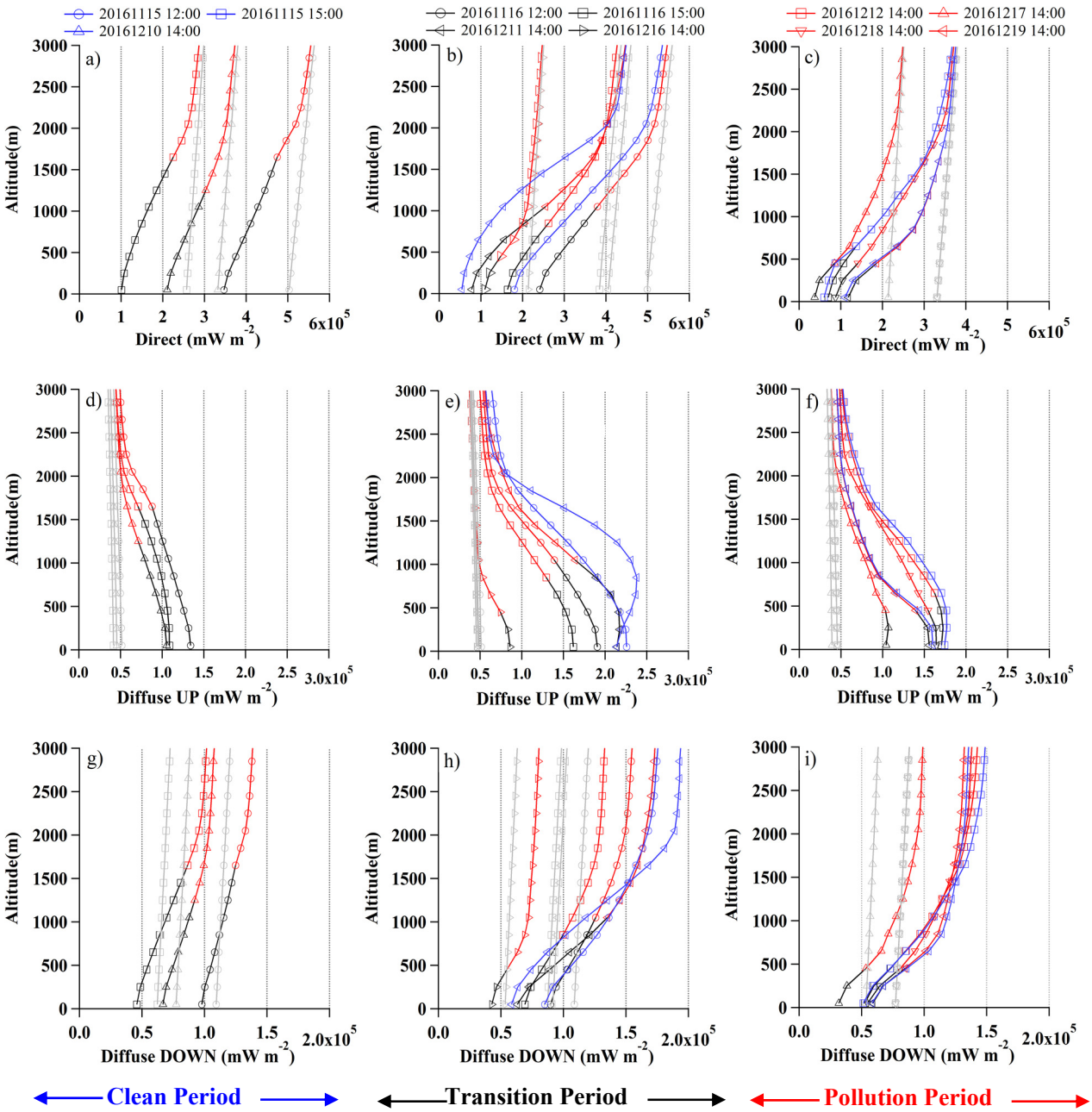

Fig. 6. Radiative transfer results calculated by DISTORT. a)-c), b)-e), and g)-i) show the direct, diffuse upward and diffuse downward irradiance respectively. The left, middle and right panel represent for CP, TP and HP period respectively, with black and red lines denoting above and within the PBL. The

colored and grey lines denote the profiles for with and without aerosol influence, respectively, and the blue lines are for corrected hygroscopic effect.

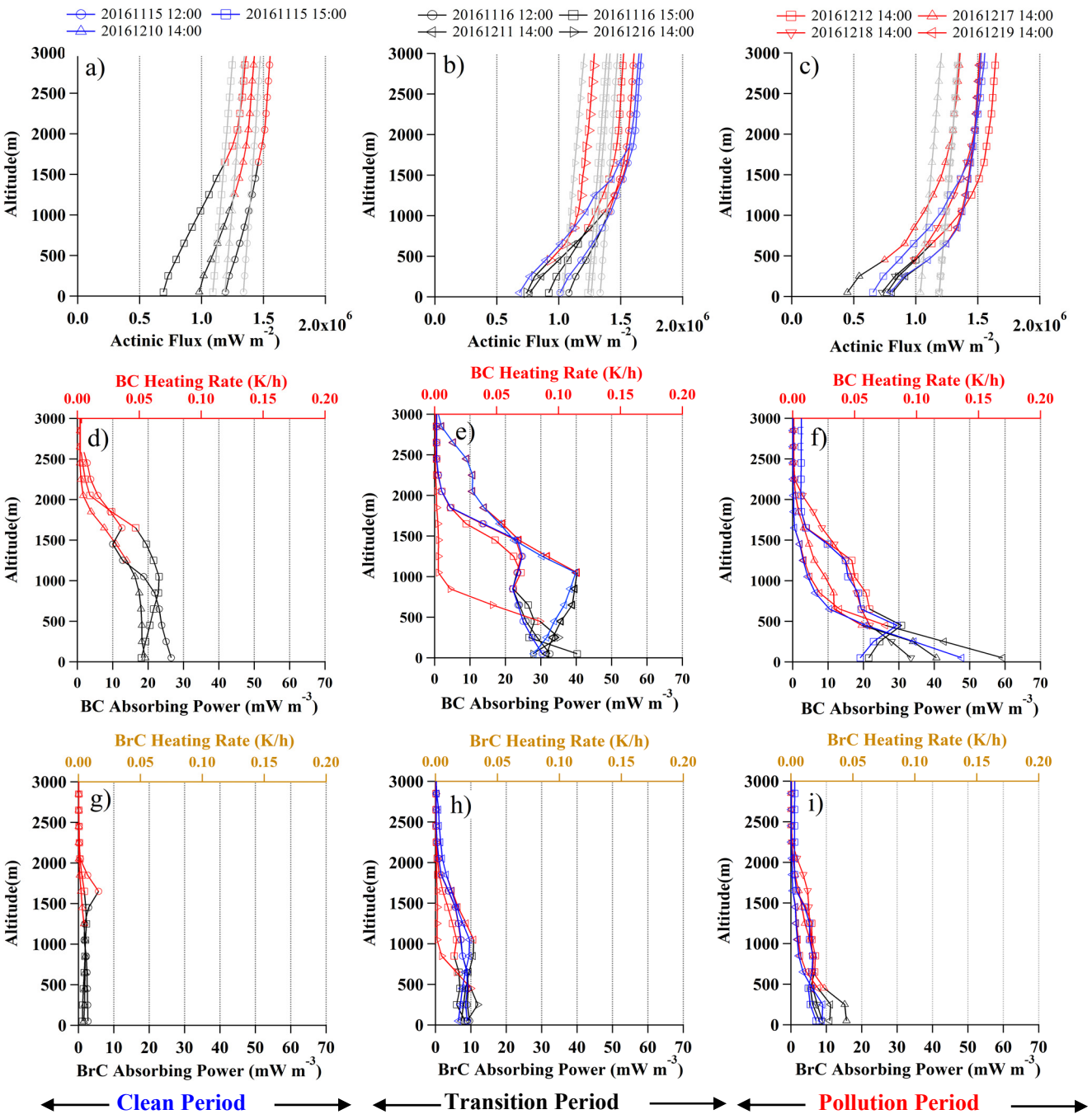

Fig. 7. Actinic flux (a-c), BC absorbing power (d-f) and BrC absorbing power (g-i). The left, middle and

right panel was for LP, TP and HP respectively, with the black and red line denoting within and above the PBL. The gray lines in a) to c) show the aerosol free results and the blue line denote the corrected hygroscopic effect. The upper x-axis from d) to i) shows the heating rate.

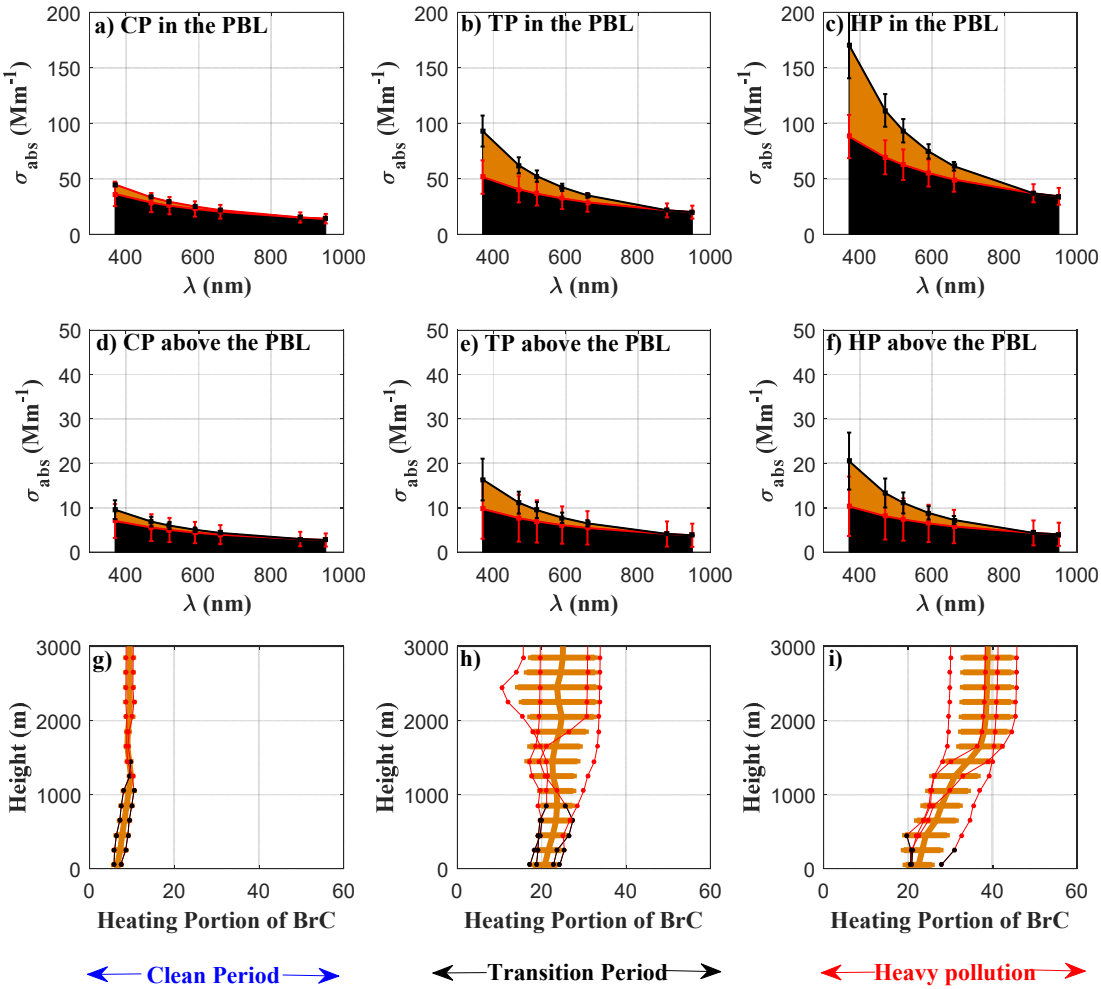

Fig. 8. Spectral absorption coefficient of BC and BrC inside and above the PBL for CP (a, d), TP (b, e) and HP period (c, f), respectively, shown in black and brown carbon color respectively. The vertical profiles of heating portion of BrC for CP, TP and HP period are shown in g) – i).